The indication of Martian gully formation processes by slope–area analysis

Susan Conway, Matthew Balme, John Murray, Martin C Towner, Chris H Okubo, Peter M Grindrod

1 **The indication of martian gully formation processes by slope-area analysis.**

2 *Susan J. Conway

3 **Work done at:** Earth and Environmental Sciences, Open University, Walton Hall, Milton

4 Keynes MK7 6AA UK tel:+44 (0)1908 659777 fax:+44 (0)1908 655151

5 **Now at:** Laboratoire de planétologie et géodynamique, CNRS UMR 6112, Université de

6 Nantes, 2 rue de la Houssinière, BP 92208, 44322 Nantes cedex, France tel : +33 (0)251

7 125570 Susan.Conway@univ-nantes.fr

8

9 **Matthew R. Balme**

10 Earth and Environmental Sciences, Open University, Walton Hall, Milton Keynes MK7 6AA

11 UK tel:+44 (0)1908 659776 fax:+44 (0)1908 655151 m.r.balme@open.ac.uk

12

13 **John B. Murray**

14 Earth and Environmental Sciences, Open University, Walton Hall, Milton Keynes MK7 6AA

15 UK tel:+44 (0)1908 659776 fax:+44 (0)1908 655151 j.b.murray@open.ac.uk

16

17 **Martin C. Towner**

18 Impacts and Astromaterials Research Centre, Department of Earth Science and Engineering,

19 Imperial College London, SW7 2AZ, UK. tel:+44 (0)20759 47326 fax:+44 (0) 20 7594 7444

20 m.towner@imperial.ac.uk

21

22 **Chris H. Okubo**

23 Astrogeology Science Center, U.S. Geological Survey 2255 N. Gemini Dr.

24 Flagstaff, AZ 86001, USA tel:+1 (928) 556-7015 fax:+1 (928) 556-7014 cokubo@usgs.gov

25

26 **Peter M. Grindrod**

27 Department of Earth Sciences, University College London, Gower Street, London WC1E

28 6BT UK tel:+44 (0)20 7679 7986

29 p.grindrod@ucl.ac.uk

30

31 *Corresponding author (e-mail: s.j.conway@open.ac.uk)

32

33

34   Number of words: 12 624

35   Number of References: 180

36   Number of Tables: 2

37   Number of Figures: 11

38   The styles for each heading level:

39   **Heading 1**

40   ***Heading 2***

41   *Heading 3*

42   Running title: Martian gully formation processes.

43

Abstract

The formation process of recent gullies on Mars is currently under debate. This study aims to discriminate between the proposed formation processes: pure water flow, debris flow and dry mass wasting, through the application of geomorphological indices commonly used in terrestrial geomorphology. We used high resolution digital elevation models of Earth and Mars to evaluate the drainage characteristics of small slope sections. We have used the data from Earth to validate the hillslope, debris flow and alluvial process domains previously found for large fluvial catchments on Earth, and have applied these domains to gullied and ungullied slopes on Mars. In accordance with other studies our results indicate that debris flow is one of the main processes forming the martian gullies that we studied. The source of the water is predominantly distributed surface melting, not an underground aquifer. We also present evidence that other processes may have shaped martian crater slopes, such as ice assisted creep and solifluction, in agreement with proposed recent martian glacial and periglacial climate. Our results suggest that, within impact craters, different processes are acting on differently oriented slopes, but further work is needed to investigate the potential link between these observations and changes in martian climate.

62   Martian "gully" landforms were first described by Malin & Edgett (2000) and defined as

63   features that have an alcove, channel and debris apron with the general appearance of gullies

64   carved by water. Within this definition gullies have a wide range of morphologies (Fig. 1)

65   and they are found in abundance on steep slopes at mid latitudes in both hemispheres on Mars

66   (e.g., Heldmann & Mellon 2004; Heldmann *et al.* 2007). They are interpreted to be

67   geologically young features because of the pristine appearance and paucity of superposed

68   impact craters. Recent work has suggested that some gullies have been active in the last

69   3 - 1.25 Ma (Reiss *et al.* 2004; Schon *et al.* 2009). Malin *et al.* (2006) observed new, high-

70   albedo, dendritic deposits (named light-toned deposits) located along the paths of some

71   gullies, and which formed between subsequent images taken by the Mars Orbiter Camera

72   (MOC). These light-toned deposits have been attributed to either dry mass wasting (Pelletier

73   *et al.* 2008; Kolb *et al.* 2010), or debris flow (Heldmann *et al.* 2010), involving up to 50 %

74   water (Iverson 1997). However, the origins of these deposits are still under debate and it is

75   not clear whether they are related to the formation processes of the gullies, or whether they

76   are formed by a secondary process.

77   The formation process for martian gullies in general is also still under debate. Three

78   main candidates exist: (1) aquifer outflow, (2) surface melting, or (3) dry granular flow. In

79   the aquifer model the water is either released from a near surface confined aquifer (Malin &

80   Edgett 2000; Heldmann *et al.* 2005) or brought up from depth by cryovolcanic processes

81   (Gaidos 2001). The main criticism of the aquifer based models is their failure to explain the

82   location of some gullies on isolated hills, impact crater central peaks, mesas and sand dunes.

83   Melting of near surface ground ice or surface ice has been proposed for the formation of

84   gullies under recent obliquity excursions (Costard *et al.* 2002). There is growing support for

85   this model with the most compelling arguments being: (1) the majority of gullies exists at

86   mid-latitudes, (2) the dominance of pole-facing gullies (Balme *et al.* 2006; Dickson *et al.*

87   2007; Kneissl *et al.* 2009) and, (3) observations of coincidence with sites of seasonal surface

88   ice accumulation (Dickson & Head 2009). Granular flow has been suggested as either

89   unassisted (Treiman 2003; Shinbrot *et al.* 2004), or carbon dioxide assisted flow

90   (Musselwhite *et al.* 2001). The main criticism of the granular flow model is that it fails to

91   replicate some commonly observed features of gullies, in particular channel sinuosity and

92   complex tributary and distributary systems (McEwen *et al.* 2007).

93   There is also debate about the type of fluid involved: pure water, or brine. Whilst

94   pure water is not stable under the current surface environment on Mars, it can persist in a

95   metastable form (Hecht 2002), although its flow behaviour may be substantially different to

96   water on Earth (Conway *et al.* 2010a). Brines are a likely product of water sourced from

97   underground and, moreover, the presence of some common geological compounds can

98   substantially depress the freezing point of water (e.g., Chevrier & Altheide 2008). Brines are

99   less likely in a surface melting scenario, because water ice condensed from the atmosphere

100   will have had less opportunity to dissolve salts than an underground water body. Both pure

101   water and brine can support very high concentrations of entrained sediment, and form a flow

102   commonly termed a "debris flow". Debris flow is an attractive candidate process for forming

103   gullies, because large amounts of erosion and deposition can be brought about with only 10 to

104   50 % water content (Iverson 1997). Several authors have proposed debris flow as a potential

105   gully-forming mechanism on Mars due to the supply of loose sediment combined with the

106   steep slopes on which gullies are found (e.g., Malin & Edgett 2000; Balme *et al.* 2006). The

107   inclusion of debris might also limit evaporation and freezing of the water within the flow.

108   Debris flows on Earth are commonly triggered by sudden and intense or prolonged rainfall,

109   (e.g., Ben David-Novak *et al.* 2004; Decaulne & Sæmundsson 2007; Godt & Coe 2007;

110   Crosta & Frattini 2008; Morton *et al.* 2008) which is not a possible mechanism on Mars

111   under recent climate. However, debris flows can also be triggered by snowmelt, or melting

112   permafrost (Harris & Gustafson 1993; Decaulne *et al.* 2005). As noted by Lanza *et al.* (2010)

113   infiltration rates on Mars are likely to exceed the low discharge rates produced by a surface

114   melting source. Hence, overland flow is unlikely, unless there is a shallow impermeable

115   barrier, such as near-surface permafrost, or frozen layer formed at the base of the water flow

116   on contact with a cold substrate (Conway *et al.* 2010a). The dominance of infiltration satisfies

117   the conditions for debris flow triggering, sediment saturation and elevated pore pressures.

118   The lack of vegetation and the associated lower cohesion of the martian soil, compared to

119   Earth, potentially means that debris flows can be triggered on much lower slope gradients

120   than they are on Earth.

121   Gullies formed by dilute-water flow and debris flow on Earth can be visually very

122   similar to each other, and the basic structure of gullies can be formed by dry granular flow

123   (Mangeney *et al.* 2007). In many geomorphological problems, convergence of visual form

124   means that using images alone can make it very difficult to determine process. The ongoing

125   debate regarding the formation mechanisms of gullies on Mars is a prime example of this. For

126   example some workers have dismissed debris flow as a mechanism for forming martian

127   gullies, because they have not observed the levées that are one of the diagnostic features of

128   debris flow (e.g., Innes 1983). However, the ability to identify levées depends on viewing

129   geometry and sun angle; metre sized levées are often not visible on 25 cm/pixel air photos of

130   Earth. It is also possible that a combination of the lower gravity and different sediment type

131   on Mars means that the levées might be small compared to those on Earth.

132   The amount of water required to carve channels and transport and deposit sediment

133   differs substantially between debris flow, water or brine flow (termed "alluvial" throughout

134   the rest of this paper) and granular flow. Determining the amount of water available at the

135   martian surface is important for questions of martian climate, hydrology and the study of

136   potential martian habitats. Hence, an accurate determination of active processes is needed that

137   in turn can constrain the quantity of fluid required to form gullies. Quantitative

138   geomorphological study can provide the tools to discriminate between these three processes.

139   The recent availability of high resolution digital elevation models (DEMs) of Mars has

140   opened up the possibility of using quantitative geomorphic methods that have, until now,

141   been restricted to analysing landscapes on Earth. By taking well-developed slope-area

142   analyses and other geomorphic process indicators for the Earth and applying them to Mars,

143   this study aims to give insights into both the processes that formed the gullies on Mars and

144   the source of any water involved.

145   We used three geomorphic tools commonly applied in terrestrial geomorphology to

146   identify active processes forming gullies on Mars: slope-area plots (Fig. 2a), Cumulative

147   Area Distribution (CAD) plots (Fig. 2b) and wetness index maps. These analytical techniques

148   are described in more detail in the following sections. They are usually used to assess active

149   processes within catchment areas and other larger-scale landscape analyses. To test whether

150   they are equally applicable to smaller areas, we first applied them to five study sites on Earth

151   at an equivalent scale to gullies on Mars. Recently deglaciated areas were preferred as these

152   have: (1) a geologically short and well defined slope development history (i.e. since

153   deglaciation) and, (2) a glacial trough valley slope-profile which strongly resembles that of

154   fresh impact craters (compare relationships in Brook *et al*. (2008) and Garvin *et al*. (1999).

155   However, suitable quality data could not be found for the alluvial end-member process in

156   glacial environments, so two desert study sites were also included.

157   When we were satisfied that different geomorphic processes could be discriminated

158   on Earth using slope-area plots, CAD plots and wetness index maps, we applied these

159   analyses to slopes containing gullies on Mars.

Method

Slope-area and Cumulative Area Distribution (CAD) methods

160

161

162 The so-called "stream power law" was first proposed by Hack (1957) and has been widely

163 used to investigate landscape evolution on Earth (e.g., Kirkby *et al.* 2003; Stock & Dietrich

164 2003). It is based on the detachment and transport limited rate of bedrock erosion, otherwise

165 known as the shear-stress incision model, which is stated as follows:

166 $$S = kA^{-\theta} \tag{1}$$

167 where S is local slope, A is upslope drainage area, k is a process related constant, which is

168 different for detachment and transport cases, and θ is the concavity index, which is process

169 dependent. It has also been noted that if the drainage area is plotted against the local slope for

170 drainage basins then process domains can be defined in log-log plots as shown in Fig. 2a

171 (after Montgomery & Foufoula-Georgiou 1993). These process domains were initially

172 schematic, based on few data, but have been supported by later work (e.g., Whipple & Tucker

173 1999; Snyder *et al.* 2000; Kobor & Roering 2004; Marchi *et al.* 2008). Brardinoni & Hassan

174 (2006) added an additional domain in which systems dominated by debris flow deposition,

175 occupy that part of the alluvial domain of Montgomery & Foufoula-Georgiou (1993), which

176 is located towards higher drainage areas and steeper slopes (Fig. 2a). This domain was

177 proposed from field observations in glacially modified area and has since been supported by

178 additional observations by Mao *et al.* (2009) in a different geomorphic setting. Process

179 information can be obtained both from the position of the data points relative to defined

180 domains on this slope-area plot, and from the trend of the data within these domains, for

181 example, whether the data points plot in a concave, convex, upward trending, or downward

182 trending curve (Tucker & Bras 1998). The general trend for an alluvial system is shown in

183 Fig. 2a, which passes through several process domains. The data for such plots are generally

184   derived from digital elevation models or topographic maps. The slope and contributing area

185   data are either extracted from the channel only, or the whole drainage basin, depending on the

186   focus of the study. In Fig. 2a these data are taken from every pixel contained within the

187   catchment of the whole fluvial system (encompassing valley hillslopes, tributaries, main

188   channels and estuary system) sampled at a single point in time.

189   Cumulative Area Distribution (CAD) is the probability distribution of points in the

190   landscape having a drainage area greater than any particular area, A^*. The log-log plot of

191   $P(A>A^*)$ against A^* gives information on the processes acting within a catchment (Perera &

192   Willgoose 1998; McNamara *et al.* 2006). Interpretation of this index varies, but generally it is

193   split into three areas: (1) at small drainage areas the plot usually evolves from convex to

194   concave, and represents diffusive erosion, (2) intermediate drainage areas are linear in a log-

195   log plot and this is thought to represent incision, (i.e. channel formation), and (3) at large

196   drainage areas there are small steps where major tributaries join the channel (Fig. 2b).

197   McNamara *et al.* (2006) split domain (1) into three sub-domains (Fig.2b): (1a) a convex

198   section, representing hillslopes that diverge and do not gather drainage, (1b) linear and steep

199   section in a log-log plot, indicating hillslopes with convergent topography and, (1c) a

200   concave section, which they suggest is a reach dominated by pore pressure triggered

201   landsliding (including debris flows which are triggered by this mechanism).

202   The stream-power law (Eq. 1), and process interpretations in slope-area and CAD

203   plots of Montgomery & Foufoula-Georgiou (1993), Brardinoni & Hassan (2006) and Tucker

204   & Bras (1998) are based on empirical hydraulic geometry functions that are predicated on,

205   and developed for, studies of large fluvial systems with channel morphology well-adjusted to

206   perennial discharge. It could therefore be argued that these systems are unlike the hillslope

207   systems in this study. Hence, we have tested these interpretive analysis techniques on small

208   gully-systems on Earth where we know the active processes in order to demonstrate that they

209 can still be valid. It is, of course, necessary to bear in mind that there is always some

210 uncertainty in inferring process from landscape form, in part due to the intrinsic variability

211 and complexity of natural systems but also due to the effects of vegetation, tectonics, climate

212 and perhaps human interaction with the landscape. However, on Mars the surface processes

213 are likely to be simpler, with little chance of factors, such as rain, vegetation or human action

214 confounding the process domains, so these indices should provide an important addition to

215 the "visual" morphology when inferring process from form.

Application of slope-area method to Mars

217 The reduced gravitational acceleration of Mars shifts the slope-area boundary of the alluvial

218 slope-area domain vertically (dotted line in Fig. 2a). This means that the unchanneled domain

219 extends to higher slopes for a given drainage area for Mars (extending into the alluvial and

220 debris flow domains for Earth); however the hillslope domain is unaffected. Considering the

221 fact that gullies on Mars do not have large tributary-channel networks it seems unlikely that

222 this domain would be well developed. Appendix 1 gives details of the calculations performed

223 to account for the gravitational acceleration of Mars. The relative gradients and curvatures of

224 the trends described by the alluvial data in slope-area plots are unaffected by the reduced

225 gravity. We have not been able to revise the position of the domain added by Brardinoni &

226 Hassan (2006) as a function of gravitational acceleration because this domain was added

227 empirically, based on field observations.

228 The slope threshold for dry mass wasting or landsliding in loose material is the same

229 as on Earth (Moore & Jakosky 1989; Peters *et al.* 2008). The slope thresholds for pore

230 pressure failure are also unaffected by the difference in gravitational acceleration. Hence

231 there would be no change to these process domains or trends for either dry mass wasting or

232 pore pressure triggered processes such as debris flow.

233   We note that on Earth, vegetation cover, soil type and geology can have profound

234   impacts on the slope values in a landscape for a given drainage area (Yetemen *et al.* 2010),

235   but we would expect only variations in soil type and geology to affect the data on Mars.

236   Despite these differences in surface properties, basins with similar processes on Earth show a

237   similar pattern or trend of data, but displaced vertically in slope-area plots (Yetemen *et al.*

238   2010).

Datasets and generation of digital elevation models

240   Slope-area analysis is only possible with high quality elevation data, preferably at a

241   resolution better than 10 m per pixel, or 1:25 000 map scale (Montgomery & Foufoula-

242   Georgiou 1993; Tarolli & Fontana 2009). For each of the terrestrial sites 1 m resolution

243   DEMs were derived from airborne laser altimeter (LiDAR) data. These were then

244   resampled to 5 m resolution to match the Mars data, as described below. Table 1 lists the

245   data sources for the study sites on Earth. The DEM for NW Iceland was produced from the

246   raw LiDAR point data collected by the UK's Natural Environment Research Council's

247   Airborne Research and Survey Facility in 2007 using techniques described by Conway *et*

248   *al.* (2010b) and correcting for between-track shifts using methods developed by Akca

249   (2007a, b).

250   For Mars we used four 1 m resolution DEMs produced using stereo photogrammetry

251   from 25 cm per pixel High Resolution Science Imaging Experiment (HiRISE) images. The

252   DEMs for sites PC, GC, KC and TS were produced by the authors from publically released

253   HiRISE images using methods described by Kirk *et al.* (2008). Significant metre-scale

254   random noise present in the DEMs of sites GC, KC and TS had a detrimental effect on

255   preliminary slope-area analyses. Hence, all the DEMs were resampled to 5 m per pixel before

256   the reanalysis was performed.

257   The precision of elevation values in the DEMs used here can be estimated based on

258   viewing geometry and pixel scale. For the DEM of site PC, the attendant image pair

259   PSP_004060_1440 (0.255 m/pixel) and PSP_005550_1440 (0.266 m/pixel) have a 12.6º

260   stereoscopic convergence angle. Assuming 1/5 pixel matching error and using a pixel scale of

261   0.266 m/pixel from the more oblique image, the vertical precision is estimated to be ~ 0.24 m

262   (cf. Kirk *et al.* 2008). DEMs for sites GC, KC and TS have a similar magnitude of vertical

263   precision. The pixel matching error is influenced by signal-to-noise ratio, scene contrast and

264   differences in illumination between images. Pattern noise can also be introduced by the

265   automatic terrain extraction algorithm, especially in areas of low correlation. Manual editing

266   is necessary to correct spurious topography in areas of poor correlation (e.g., smooth, low

267   contrast slopes and along shadows).

268   Finally, a synthetic crater was constructed to test whether the results from the Mars

269   study sites in general reflected the process, or instead were a result of the geometry imposed

270   by the impact crater setting (all the Mars study areas were on the inner walls of bowl shaped

271   depressions, but none of the ones on Earth were). A 10 km diameter synthetic crater was

272   created by applying a smooth parabolic radial profile, which was derived by fitting curves

273   through ungullied radial profiles of the craters in sites PC and GC. Metre-scale "pink" (also

274   called "1/f") noise was added to simulate a natural rough surface (Jack 2000).

275 ### *Derivation of drainage area and local slope*

276   Representative slope sections were chosen in each DEM (Figs. 3 and 4). For Earth, these

277   were chosen to represent end member and intermediate process domains, including dry mass

278   wasting, debris flow and alluvial processes. On Mars, some areas were chosen that covered

279   the complete slope on which gullies are found, whilst others covered a single gully system, or

280   ungullied slope for comparison. Slope sections always included the drainage divide at the top

281   and extended downslope as far as the visible signs of the distal extent of the gully (or slope)

12

282   deposits. Where possible lines delineating drainage basins were followed to define the lateral

283   extent of slope sections, but on poorly incised hillslopes this was not always possible and the

284   lateral extent was defined as a straight line. For site KC, on Mars, we chose different

285   configurations of slope sections to test the sensitivity of our analyses to the exact method

286   used to delineate the slope-sections. Careful delineation of slope sections is necessary for two

287   reasons. Firstly, because the larger the sample area, the more processes are included within it,

288   and the more difficult the results will be to interpret. Secondly, if parts of the slope that are

289   integral to the process to be identified are omitted, then the process signal will not be

290   complete.

291   The slope and the flow directions of each pixel in each DEM were determined using

292   a "Dinf" algorithm. This algorithm gives flow directions in any direction, rather than only

293   towards one of the eight neighbouring pixels (Tarboton *et al.* 1991). This has been shown to

294   produce better results from slope-area analysis because it gives a more accurate

295   approximation of the real path of flow through the landscape (Borga *et al.* 2004). For each

296   pixel, the accumulation of flow was calculated from the flow directions by summing the

297   number of pixels located upstream, and multiplying by the pixel area. These analyses were

298   performed using the TauDEM extension for ArcGIS, based on the algorithms developed by

299   Tarboton (1997). For each DEM the "wetness index" was also calculated. This is the natural

300   logarithm of the ratio of contributing area to slope. It provides information on the potential

301   connectivity of the landscape drainage and the potential ability of the surrounding landscape

302   to route drainage (Woods & Sivapalan 1997). However, in the case of Earth and particularly

303   in the case of Mars this index should not be interpreted literally as implying that the terrain is

304   "wet". In our study it is used as a visual aid to interpret the spatial variability of the slope-

305   area plot. For example, highly permeable talus slopes on Earth are essentially dry, but they

306   may have moderate to high wetness index. However, we would expect a talus slope on Earth

307 to show a characteristic spatial pattern of wetness index, indicative of dry mass wasting

308 processes. All the DEMs underwent the same processing steps.

309 　　　　We extracted the drainage area and slope for every pixel within the chosen slope

310 sections. To simplify the representation of these data we calculated the mean slope for 0.05

311 wide logarithmic bins of drainage area, and then constructed the slope-area and CAD plots.

312 Binning data in this way make the trends in slope-area and CAD plots clearer and is a

313 commonly used display technique (e.g., Snyder *et al.* 2000).

314 　　　　In addition, for one site on Mars (site KC), we visually identified the initiation sites

315 of the gullies on orthorectified HiRISE images. The initiation points for the gullies were

316 defined as the furthest upstream extent defined by a distinct cut, or scarp (Fig. 5a). For each

317 of these locations we extracted the slope and drainage area for the underlying pixel. This

318 analysis was not performed for site PC because edge contamination and noise made it

319 impractical. The analysis was also omitted for site GC because the gullies start at the top of

320 the slope, so would by definition occur at the lowest drainage areas.

Study areas

Earth

323 All the study sites on Earth are located in the northern hemisphere and most are within the

324 continental USA. Table 1 provides a summary of the sites and Fig. 3 shows the setting of the

325 areas studied.

Site SJ – San Jacinto, California

327 This site is located in California along a splay of the San Andreas fault, called the San Jacinto

328 fault. This area is a desert with little rainfall (~ 150 mm, annual average recorded by NOAA

329 weather station in nearby Borrego Springs), which has undergone rapid recent uplift caused

14

330   by the fault system. The landscape has a well developed ephemeral gully network with large

331   alluvial fans. From the study of the 1 m LiDAR data and aerial images we infer the processes

332   forming these fans to be sheet-flow rather than debris flow, based on the lack of levées and

333   lobate terminal deposits. The vegetation is sparse, consisting of small scrub bushes. The

334   underlying geology of the study area is mainly granite, schist and gneiss with minor outcrops

335   of Quaternary older fan deposits (Moyle 1982). For our analyses we used three study areas

336   that contained small complete gully systems, including sources, channels and debris aprons,

337   but avoided large fan systems and debris aprons from neighbouring systems (Figs. 3a and 3b:

338   study areas SJ1, SJ2 and SJ3). Due to the small size of the fans in area SJ1 it is difficult to

339   entirely rule out debris flow as a potential process in forming these alluvial fans.

340   *Site DV - Death Valley, California*

341   This site is located a few kilometres NE of Ubehebe volcano, in Death Valley, California.

342   This is a desert area that has well developed ephemeral gully networks with large alluvial

343   fans. There is little precipitation in this area although the nearby mountains receive as much

344   as 85 mm of rain per year (Crippen 1979) and rare large storms can do much geomorphic

345   work. Debris flows are found on the fans in the area (e.g., Blair 1999, 2000), but the primary

346   process active in the gullies is alluvial transport (Crippen 1979). We inspected the 1 m

347   LiDAR data for presence of levées and depositional lobes on the fans and found no evidence

348   of these. However, without direct field observations the fact that debris flows do not act on

349   these fans remain an assumption. The bedrock consists of Palaeozoic sedimentary rocks

350   (Workman *et al.* 2002). We chose two study areas (Fig. 3c: study areas DV1 and DV2) with

351   gully systems that were not affected by neighbouring alluvial fans or gully systems so only

352   receive local rainfall levels.

353   *Site KA – St Elias Mountains, Alaska*

354   This site is located east of the abandoned town of Katalla close to the recently deglaciated

355   mountain range of St Elias, near the coast of Alaska and on the border with Yukon, Canada.

356   The area has been unglaciated for approximately the last 10 000 years (Sirkin & Tuthill 1987)

357   and receives very high precipitation, which falls as snow on the upper slopes and rain on the

358   lower. Our study area overlies Tertiary volcanic materials. The slope scarp was generated by

359   the active Ragged Mountain Fault (Miller 1961). The area was neither snow covered nor tree

360   covered at the time of survey and the slopes are composed of steep bedrock cliffs that lead

361   directly into large talus aprons. Debris flow tracks are apparent across this talus slope,

362   especially in study areas KA3 and KA4, and might have occurred in study area KA3 as well

363   (Fig. 3d). Study area KA1 has no evidence of debris flow processes (Fig. 3d).

364   *Site FR – Front Range, Colorado*

365   This site is located in the mountainous eastern side of the continental divide. The area was

366   deglaciated around 14 000 to 12 000 years before present (Godt & Coe 2007) and the

367   landscape is dominated by glacially carved valleys. This area has experienced recent debris

368   flows (Coe *et al.* 2002; Godt & Coe 2007) and has no permanent snowpack. Our study

369   slopes, located above the tree line, are dominated by Precambrian biotitic gneiss and quartz

370   monzonite, scattered Tertiary intrusions, and by various surface deposits, all of which host

371   debris flows (Godt & Coe 2007). The head and sidewalls of the cirques have large rockfall

372   talus deposits and which have also experienced recent debris flows. These slopes have little

373   or no vegetation. Three of our study areas (Figs. 3e and 3f: study areas FR2 to FR4) include

374   debris flows located on talus. By way of contrast, we also examined a partially vegetated

375   slope (study area FR1) that is unchanneled and which we infer to be dominated by creep

376   processes (Fig. 3e).

377 *Site WF – Westfjords, Iceland*

378 The site is located in NW Iceland and is dominated by fjords and glacially carved valleys.

379 The last glacial retreat occurred approximately 10 000 years before present (Norðdalh 1990).

380 The valley walls have many active debris flows (Conway *et al.* 2010b) and on the slopes

381 above Ísafjörður (Fig. 3g: study area WF1) they occur in most years (Decaulne *et al.* 2005).

382 The site has a maritime climate, so has high levels of both snow and rainfall, but does not

383 have permanent ice or snow patches. The site is underlain by Miocene basalts, although the

384 debris flows occur most often in glacial till. From this site we chose a study area above the

385 town of Ísafjörður that has very active debris flows (Fig. 3g: study area WF1), two study

386 areas with less active debris flows and more alluvial processes (Figs. 3g and 3h: study areas

387 WF2 and WF3), and one study area dominated by rockfall and rock slide processes, although

388 there are some debris flow tracks visible in the field (Fig. 3h: study area WF4). All these

389 study areas have patchy vegetation, but no trees.

390 **Mars**

391 All the gullies that we studied on Mars were located on the inner walls of craters in the

392 southern hemisphere (Table 2). Slopes both with and without gullies were analysed for

393 comparison. Sites PC, GC and KC were analysed by Lanza *et al.* (2010), because all the sites

394 showed visual evidence of debris flows.

395 *Site PC – Penticton Crater in Eastern Hellas*

396 This site contains the very recent, light-toned deposits observed by Malin *et al.* (2006) and

397 interpreted by them to be a recent "gully forming" event. These flows were later suggested by

398 Pelletier *et al.* (2008) to be produced by dry granular flow, or possibly also debris flow. This

399 slope does not have any well defined channels. We used two study areas within the ~ 7.5 km

400 diameter crater for our slope-area analyses, shown in Figs. 4a and 4b. Study area PC1 is

401   located over the equator-facing light-toned deposits (Fig. 4a) and study area PC2 on the west-

402   facing crater wall which contains small gullies (Fig. 4b). These gullies appear to be incised

403   into "mantle deposits" (Mustard *et al.* 2001). The mantle is hypothesised to be the remnants

404   of a previously extensive volatile rich deposit (e.g., Mangold 2005). This crater is very

405   asymmetric, with the east and north rims being subdued in terms of elevation (the rim is

406   nearly absent on the east side) whilst the southern rim is abrupt and steep.

407   *Site GC – Gasa Crater in Terra Cimmeria*

408   This ~ 7 km wide crater, shown in Figs. 4c and 4d, has well developed alcoves or

409   indentations into the rim of the crater. Gully channels are most obvious on the west-facing to

410   pole-facing slopes (Figs. 4c and 4d) and the equator-facing slope lacks these well defined

411   alcoves and channels (Fig. 4e). We chose sections on the pole- (study areas GC1 and GC2),

412   west- (study area GC3) and equator-facing (study area GC4) slopes. This crater is located

413   within a larger crater, which also has gullies on its west- to pole-facing slopes. There is no

414   evidence of mantle deposits being present anywhere within this crater.

415   *Site KC – crater inside Kaiser Crater in Noachis Terra*

416   The study crater, ~ 12 km across is located within the larger Kaiser crater, which not only has

417   gullies down its own rim, but also gullies on the dunes within it (Bourke 2005). Gullies in

418   this crater have alcoves at various positions on the slope, which converge to form well

419   defined tributary networks. Lateral levées bound some of the channels (Figs. 5b and 5c). This

420   slope has the subdued appearance often attributed to the presence of volatile rich mantle

421   deposits (Mustard *et al.* 2001). We chose study areas that encompass the drainage area of two

422   gullies (study area KC2), a single gully (study area KC1) and also the slope section as a

423   whole (study area KC3), all of which are shown in Fig. 4f. We chose study area KC4, an area

424   of the slope not affected by gullies, for comparison (Fig. 4f).

Site TS – crater in Terra Sirenum

426 This ~ 7 km diameter crater is located to the south of Pickering Crater in Terra Sirenum and

427 contains pole-facing gullies. We analysed an equator-facing slope (Fig. 4g: study area TS1)

428 which has no evidence of channels but contains an apparently well developed talus apron.

429 There is no evidence of mantle deposits being present on this slope.

430 **Results**

431 *Earth*

432 Initially we chose two study areas with talus and with active creep. The slope-area analysis

433 results for these are shown in Fig. 6a. The study areas with well developed talus (WF4 and

434 KA1) show the following pattern on log-log plots: (1) At small drainage area the curves are

435 initially flat. (2) There is then a linear decrease in slope with increasing drainage area. (3) The

436 curve then becomes horizontal again at higher drainage area with a lower slope value. Talus

437 slopes that have a mixture of processes (e.g., KA2) show a curve that drops off linearly in

438 log-log plots then flattens at higher drainage areas.

439 The CAD plot (Fig. 7a) provides additional information: the talus dominated study

440 areas have a very smooth convex shape. The gradient of the curve is low until the drainage

441 area is between approximately 0.001 km^2 after which the curve drops sharply and continues

442 to steepen with increasing drainage area.

443 The soil creep diffusive process study area (FR1 in Fig. 6a) shows a distinctive

444 signature in slope-area plots: (1) The curve is initially horizontal to gently downwards

445 sloping. (2) Between drainage areas of 0.0001 to 0.001 km^2 the slope increases linearly with

446 increasing drainage area. (3) There is then a marked slope turnover at which the curve

447 switches to decreasing slope with increasing drainage area. The soil creep diffusive process

448 study area resembles the talus slopes in CAD plots (FR1, Fig. 7a).

449   Figs. 6b and 7b show the debris flow study areas that are influenced by talus

450   processes and Figs. 6c and 7c show those that are more influenced by alluvial processes.

451   Generally in slope-area plots debris flow produces a curve that drops off linearly in log-log

452   plots, flattening off before finally dropping away steeply. The difference between the talus

453   study areas (e.g. KA2, Fig. 6a) and the debris flow study areas influenced by talus (Fig. 6b) is

454   subtle in some cases. In a similar way the difference between the debris flow areas influenced

455   by talus processes (Fig. 6b) and those influenced by alluvial processes (Fig. 6c) is also subtle.

456   Without field information it would be difficult to differentiate talus dominated and debris

457   flow dominated slopes reliably in slope-area plots (e.g., compare Figs. 6a, KA2 and 6b).

458   However, in CAD plots it is possible to differentiate between the two process types. The

459   debris flow dominated study areas (Figs. 7b and 7c) show the following pattern: (1) The

460   curve drops away from the horizontal slowly (but faster than the talus slopes) at small

461   drainage areas. (2) The curve then either dips down linearly, or follows a flattened convex

462   path, and (3) at high drainage areas the curve drops away sharply with increasing drainage

463   area.

464   Study areas modified by ephemeral water flow have distinct signatures in slope-area

465   plots (Fig. 6d) and in CAD plots (Fig. 7d). In slope-area plots they show a shallow linearly

466   decreasing trend at small drainage areas, which gets steeper at higher drainage areas, and

467   drops into the alluvial domain. The CAD plot drops away from the horizontal slowly and then

468   dips down linearly (or even with a concave profile) until the tail of the curve drops sharply

469   off at the highest drainage areas.

470   *Synthetic Crater*

471   The slope-area and CAD plots for the synthetic crater are easily differentiated from the

472   process study areas that we have examined on Earth. In slope-area plots the synthetic crater

473   produces a hump-backed curve (Fig. 8d): at small drainage areas the curve rises steeply, then

474 levels off and drops at high drainage areas. In appearance the curve is, as expected, nearest to

475 study area FR1, the area dominated by diffusive creep (Fig. 6a). In CAD plots (Fig. 9d) the

476 line follows a smooth convex arc, similar to that shown by talus on Earth, except without a

477 break in gradient.

478 *Mars*

479 The slope-area plots for sites PC and GC (Penticton Crater and Gasa Crater inner slopes)

480 closely resemble each one another (Fig. 8a and b). The resulting curve can be divided into

481 three zones: (1) A short initial increase in slope with increasing drainage area, followed by a

482 slope turnover at very small drainage areas. (2) A linear or slightly concave decreasing slope

483 trend with increasing drainage area that continues for most of the plot. (3) Finally, at the

484 largest drainage areas, there is a steep decrease in slope with increasing drainage area. For

485 study area PC1 there is a distinct and linear decline in slope with drainage area, whereas for

486 study areas PC2, GC1, GC2 and GC3 this section is slightly concave. The drop-off at the

487 highest drainage areas occurs at lower absolute drainage area values than for site GC. In the

488 CAD plot, study areas PC1 and GC4 have a smooth convex form, whereas study areas PC2,

489 GC1 and GC2 all have a nearly linear, flattened section at intermediate drainage areas (Figs.

490 9a and 9b). Study area GC3 lies close to PC1, GC1 and GC2 but without any sign of

491 flattening.

492 The slope-area plots for gullies in study areas KC1, KC2 and KC3 (Fig. 8c) can be

493 split into three sections as follows: (1) at small drainage areas the curve is sub-horizontal with

494 a subtle upward trend. This trend is more apparent for the data from individual gullies than

495 the data obtained from the whole slope section and is somewhat variable between gully

496 systems. (2) At intermediate drainage areas there is a transitional zone, occurring at different

497 drainage areas for each gully system, in which slope drops off markedly with drainage area.

21

498   (3) At higher drainage areas there is a gently declining relationship between slope and

499   drainage area, which is the same for all the gully systems.

500   The ungullied study area (KC4) is also shown in Fig. 8c. This study area has a

501   hump-back shape, resembling that seen for the synthetic crater. The hump occurs across the

502   same slope values as the transition zone (2) for the gullied slopes. In CAD plots (Fig. 9c)

503   study areas KC2 and KC3 have a flattened section at intermediate drainage areas, followed

504   by a steepening decrease at higher drainage areas. The study area without gullies (KC4) has a

505   curve that is convex and initially declines slowly, before dropping off steeply. Study area

506   KC1 has a less flattened profile than study areas KC2, or KC3 and it seems to be a mixture

507   between slope types typified by gullied study areas KC2 or KC3 and ungullied study area

508   KC4.

509   In slope-area plots, study area TS1, an ungullied slope, shows a slope-area turnover

510   at small drainage areas, followed by a decreasing and slightly concave trend in slope with

511   drainage area (Fig. 8d). There is a slight upturn at the highest drainage areas, but this is likely

512   to be an artefact caused by few data-points being used to calculate the mean slope in these

513   bins. In CAD plots (Fig. 9d) study area TS1 has a very smooth convex curve.

514   The slope and drainage area of the gully head initiation points were recorded for site

515   KC. These data are displayed on Fig. 8c. Interestingly, the locations of the gully heads cluster

516   around the range of drainage areas of the transitional section in the slope-area plot, but are

517   located at higher slope values.

518   ***Wetness Index on Earth and Mars***

519   The spatial distribution of the slope-area data is most easily visualised using a wetness index

520   map. Maps of wetness index are presented for Earth (Fig. 10) and for Mars (Fig. 11). The

521   alluvial study areas in Earth sites SJ and DV show very low overall wetness indices – only

522   the channels have significant wetness index (Figs. 10a, 10b, and 10c). Debris flow study

523   areas are slightly more complex (Figs. 10d, 10e, 9f, 10g, and 10h): the slopes generally have

524   moderate wetness index, but there are localised paths along which the wetness index is

525   higher. Site WF (Figs. 10g and 10h) is the best example of this pattern, but it is also the area

526   with the highest influence of overland flow. For site KA (Fig. 10d) this signature is poorly

527   developed, but this site has been influenced by talus processes. The creep dominated study

528   area, FR1, has moderate wetness index throughout (Fig. 10e). The talus study areas KA1,

529   KA2 (Fig. 10d) and WF4 (Fig. 10h) show lobe-like areas of low wetness index with widening

530   streaks of higher wetness index in between.

531   On Mars, study area PC1 (Fig. 11a) and the synthetic crater (Fig. 11h) have similar

532   wetness index maps: the slope generally increases in wetness index going downhill and there

533   are quasi-linear streaks of higher wetness index that increase in value going downslope.

534   Study area PC2 (Fig. 11b) has overall low wetness index, apart from concentrated lines of

535   high wetness index within the gully alcoves, that spread and become more diffuse in the

536   debris aprons. A similar overall pattern is shown for study areas GC1, GC2 and GC3 (Figs.

537   11c and 11d), but the ridges around the alcoves have very low wetness index. Study area GC2

538   in particular (Fig. 11c) shows very concentrated slightly sinuous high wetness index lines on

539   its debris apron. However this part of the DEM contains significant noise, making it hard to

540   judge whether this is simply an artefact. Study areas GC4 (Fig. 11e) and TS1 (Fig. 11g) have

541   similar wetness index maps: there is low wetness index at the crest of the slope and where

542   bedrock is exposed and the wetness index generally increases downslope, but this trend is

543   superposed with diffuse linear streaks of higher relative wetness index. Site KC (Fig. 11f) has

544   generally moderate wetness index, with the alcoves and channels of the gullies showing

545   focussed high wetness index flanked by much lower wetness index and the debris aprons

546   having generally high wetness index with diffuse downslope streaking.

Discussion

Comparison of Earth data to previously published slope-area process domains

550   There are two interlinked methods of determining slope processes from slope-area plots:

551   (1) The data points fall within domains in the plots which have been found both theoretically

552   and empirically to relate to particular processes, and

553   (2) The data points exhibit trends and gradients that provide information on active processes.

554   We compared our data from Earth to the slope-area process domains of Montgomery

555   & Foufoula-Georgiou (1993) and the additional domain added by Brardinoni & Hassan

556   (2006), shown as solid lines in Fig. 6. The data from our creep, talus and debris flow analyses

557   fall into the debris flow domain of Montgomery & Foufoula-Georgiou (1993). However,

558   some of our debris flow data drop into the alluvial domain at the highest drainage areas.

559   Because they are small systems with limited drainage areas, however, only a few points fall

560   within the alluvial domain. Some of our data approach the additional domain added by

561   Brardinoni & Hassan (2006), but do not extend towards sufficiently high drainage areas (or

562   low drainage areas) to enter it (Fig. 6b and 6c). Our data from the alluvial systems (Fig. 6d)

563   fall into both the debris flow and alluvial domains. They start to trend downwards in slope-

564   area plots at lower drainage areas than our debris flow systems.

565   Tucker & Bras (1998) simulated the effects of different dominant processes on

566   slope-area plots and we now compare their model results to the patterns in slope-area plots

567   shown by our data. Our talus systems (Fig. 6a) closely fit their model of a landscape

568   dominated by landsliding (which includes the process of debris flow). In slope-area plots our

569   talus data have an initial flat section at small drainage areas, which represents the slope

570   threshold for the rock wall failure and so differs between localities. At higher drainage areas

571   the curves are again flat, representing the failure threshold of loose talus, which is consistent

572   for all areas at approximately 0.7 gradient, equivalent to a slope of approximately 35°. This is

573   an approximate mean slope angle for talus slopes on Earth (Chandler 1973; Selby 1993) and

574   is shown by a dotted horizontal line in Figs. 6 and 8. Between these two horizontal sections

575   there is a transition where the dominance shifts from rock wall failure to unconsolidated talus

576   failure.

577   Within the framework of Tucker & Bras (1998) the pattern shown by the debris flow

578   slopes on Earth (Figs. 6b and 6c) is most consistent with the transition from unsaturated

579   landsliding (dry mass wasting of both talus and rock wall) to pore pressure triggered

580   landsliding (which we interpret to also include debris flow), in a landscape dominated by

581   landsliding. The presence of processes with a slope failure threshold cause data in slope-area

582   plots to fall along horizontal lines. Hence, as the process dominance changes from rock wall

583   failure (highest threshold) to unsaturated landsliding (intermediate threshold) to saturated

584   landsliding (lowest threshold) the curve declines and levels off at the slope value of the

585   saturated landslide threshold in that particular area. As each physical locality has its own

586   saturation threshold this horizontal section occurs at different slope values for different

587   localities but is always located below the dry stability line at 0.7.

588   In slope-area plots, our data from alluvial systems on Earth (Fig. 6d) show a simple

589   decline of slope with drainage area, possibly steepening at higher drainage areas. The data are

590   scattered at drainage areas > 0.001 km^2, due to the limitations of the small sizes of the gully

591   systems available. This means a relatively small number of pixels were used to generate each

592   point, leading to random scatter. However, even taking into account the scatter, the data are

593   below the slope threshold for dry slope failure at 0.7 gradient, which suggests a gradual

594   transition from pore pressure dominated landsliding to fluvial processes.

595   The main feature of our creep dominated hillslope data (FR1, Fig. 6a), is a turnover

596   from increasing slope with drainage area to decreasing slope with drainage area. One of the

597   alluvial systems in site SJ (study area SJ3) shows a weak slope turnover at the lowest

598   drainage areas but none of the other plots show this feature. The slope-area turnover is shown

599   in Fig. 2 and is generally expected to occur in slope-area plots (e.g., Tucker & Bras 1998). It

600   usually occurs in, or close to, the "hillslope" domain of Montgomery & Foufoula-Georgiou

601   (1993). The turnover represents a transition from convex slopes dominated by diffusive

602   processes (which include soil creep often modified by plant roots and other biota) to concave

603   slopes dominated by advective, or alluvial processes. Within the diffusive processes domain

604   in slope-area plots, slope increases with drainage area. The most likely reason that most of

605   our data do not show this turnover is that the slopes we studied lack stable vegetation

606   (Dietrich & Perron 2006; Marchi *et al.* 2008). Another potential contributing factor is that the

607   bedrock and colluvium in our study areas are not naturally cohesive, for example, clay-rich

608   rocks can exhibit convex creep-dominated slopes in unvegetated badlands on Earth.

609   The pattern of data in slope-area plots shown by our alluvial systems and some of

610   our debris flow systems (slow decline at small drainage areas followed by a steep decline at

611   higher drainage areas) has been shown from numerous remote sensing and field studies to

612   mark the transition from the colluvial (including debris flow) regime, to that of a fully fluvial

613   regime (e.g., Lague & Davy 2003; Stock & Dietrich 2003; Stock & Dietrich 2006). Some

614   have described the transition as a separate linear portion of the plot between the colluvial and

615   the fluvial (Lague & Davy 2003) and some as a gradual curved transition (Stock & Dietrich

616   2003). However, both are consistent with Tucker & Bras' (1998) transition from pore

617   pressure triggered landsliding into a fully fluvial system. Our plots do not show a well

618   developed alluvial regime, but this is due to the use of high resolution data of very small

619   areas rather than large, well developed fluvial catchments.

620   In summary, our terrestrial data are consistent with published slope-area process

621 domains, and provide reassurance that the method is applicable and that the Mars data can be

622 used to infer process in a similar way. The caveat to this is that the environmental differences

623 between Earth and Mars, as detailed in the introduction, must be considered when comparing

624 terrestrial process domains to data from Mars. Furthermore, improved process discrimination

625 can be made by considering CAD profiles in addition to slope-area analysis.

626 ### *Comparison of Earth data to published CAD process domains*

627 Comparison of all our CAD plots for Earth (Fig. 7) to the published process domains for

628 CAD (Fig. 2) reveals that our data do not generally follow the cited trends. This is possibly

629 because we are studying small areas, rather than large catchments. However, the shape of the

630 curve outlined by our data in CAD plots does allow process discrimination and does follow

631 some of the framework outlined by McNamara *et al.* (2006). Specifically region 1 on Fig. 2

632 has three sub-regions whose shapes can be recognised in our datasets. The talus data (Fig. 7a)

633 and synthetic crater (Fig. 9d) are both convex in their CAD plots, resembling most closely

634 region 1a of McNamara *et al.* (2006). They describe this region as representing "hillslopes

635 that diverge and do not gather drainage." Our alluvial data and some of our debris flow data

636 show a flattening of the CAD plot curve in the middle region, giving a steep linear section,

637 corresponding to either region 1b or region 2 (Fig. 2b) which McNamara *et al.* (2006)

638 describe as slopes that are convergent (1b), or channel forming (2). Two debris flows (WF2

639 and WF3 in Fig. 7c) show a concave section, which would correspond to region 1c of

640 McNamara *et al.* (2006) and which they attribute to pore pressure triggered landsliding or

641 debris flow.

642   The similarity of talus and debris flow in slope-area plots can be attributed to their

643 similarly linear long profiles. However, the two processes produce different patterns in CAD

644 plots because talus slopes tend to disperse drainage but debris flow slopes tend to have

645 convergent drainage. This can also be seen in the wetness index plots (Fig. 10).

646   This difference of behaviour in CAD and wetness index plots, in addition to the

647 information from the slope-area plots, shows that we can detect slopes dominated by alluvial,

648 debris flow and dry mass wasting on the basis of these parameters, even for small catchments

649 such as individual gullies or debris flow tracks. However, it should be noted here that these

650 analyses have been performed on relatively few sample sites on Earth and some of the

651 differences are subtle. Future work has to include extending this analysis to a greater number

652 of test sites on Earth to verify that this kind of process discrimination is robust. Using these

653 initial results we continue and apply these methods of process discrimination to Mars.

654 *Process domains for gullies on Mars*

655 In slope-area plots all the Mars slope sections, except study area TS1, fall below the slope

656 threshold for dry mass wasting (dotted line in the plots in Fig. 8). This means that talus-like

657 dry mass wasting is not a dominant process in these areas. However, study area TS1, visually

658 similar to talus on Earth, is not only above the slope threshold for dry mass wasting, but also

659 bears a signature similar to talus on Earth in the combination of its slope-area plot, CAD plot

660 and wetness index map

661   Within the process domains of Montgomery & Foufoula-Georgiou (1993) the

662 majority of the Mars data lie within the debris flow domain, with some data located in the

663 debris flow deposition domain added by Brardinoni & Hassan (2006) and a few in the

664 alluvial domain. The difference in gravity between Earth and Mars requires an upwards slope

665 adjustment to the alluvial channels domain boundary (see Fig. 2a) in slope-area plots

666 (Appendix 1), but does not change the gradient of the line. This is marked by the dash-dot

667 line on the plots in Fig. 8. This shift places more data in the unchanneled domain, but does

668 not place any additional data into the alluvial or debris flow domains. This in itself

669 distribution does not provide very detailed information on the formation mechanisms for

670 gullies. However, by combining slope-area trends, CAD plots and wetness index maps we

671 can make more detailed assessments. We examine each of the study areas on Mars in turn

672 and then discuss the overall implications for the gully formation processes.

673 *Synthetic Crater*

674   The pattern in slope-area plots of the interior of impact craters is, in part, a result of

675 the inherent shape of the crater slope which in turn is due to the impact process and the

676 modification that occurs immediately afterwards. The slope of a fresh impact crater is

677 concave and exponentially shaped in profile (Garvin *et al.* 1999). Thus in slope-area plots it

678 resembles a well developed alluvial system on Earth (e.g., Hack 1957). This reinforces the

679 uncertainty in inferring a unique process from slope form. In CAD plots, however, the

680 synthetic crater data show a similar pattern to that of talus slopes on Earth, indicating that at

681 short length-scales this type of slope cannot channelise flow on its own. This interpretation is

682 supported by the wetness index plot (Fig. 11), which shows a slowly coalescing flow, rather

683 than discrete areas of fluid concentration.

684 *Site PC – Penticton Crater in Eastern Hellas*

685   In slope-area plots the slope turnover is well expressed for both study areas in site

686 PC (Fig. 8a). This suggests a strong diffusive or creep influence on both slopes. Study areas

687 PC1 and PC2 both resemble either poorly developed talus or debris flow in slope-area plots.

688 In the CAD plot (Fig. 9a); however, study area PC2 has the distinctive profile associated with

689 debris flow, whereas study area PC1 more closely resembles talus. Talus processes can only

690 be active in study area PC1 at small drainage areas, where it lies on the dry mass wasting

691 threshold in slope-area plots. Hence the shape of the CAD curve must be explained by

692 another process, which has a slope threshold but does not concentrate drainage. This

693   unknown process must be pore pressure triggered as it is below the slope for dry mass

694   wasting. In addition, the wetness index plot reveals that study areas PC1 and PC2 are very

695   different: study area PC1 has a similar wetness index map to the synthetic crater (Fig. 11h),

696   whereas study area PC2 resembles debris flow areas on Earth (e.g., Fig. 10f) with strongly

697   concentrated high wetness index within alcoves and channels, becoming more diffuse down

698   slope on the debris aprons.

699   The combined evidence suggests that the west-facing slope, which contains small

700   gullies, has been modified by debris flow, whereas the equator-facing slope is more similar to

701   dry mass wasting deposits. This agrees with the interpretation of Pelletier *et al.* (2008), who,

702   using numerical modelling, concluded that the new bright toned deposits on this slope were

703   more similar in form to deposits of dry granular flows than debris flows.

704   *Site GC – Gasa Crater in Terra Cimmeria*

705   In the slope-area plot for site GC (Fig. 8b), the slope-turnover occurs at very small

706   drainage areas (one or two pixels) and is thus partly abbreviated. This suggests that creep has

707   not strongly influenced this site. This interpretation is supported by the observation that the

708   gully heads originate at the very top of the slope. Study areas GC1, GC2 and GC3 resemble

709   either poorly developed talus on Earth (study area KA2, Fig. 6a) or debris flows on Earth

710   (Figs. 6b and 6c) in slope-area plots. However, in CAD plots (Fig. 9b) they have a flattened

711   mid-section, resembling debris flow systems on Earth. Their wetness index plots (Figs. 11c

712   and 11d) have strong similarities with debris flow systems on Earth (e.g., Fig. 10g): showing

713   flow concentration in the alcove and channel with more diffuse flow on the debris apron.

714   Study area GC2 (Fig. 11c) shows a similar pattern of wetness index to the alluvial systems on

715   Earth, with focussed flow throughout.

716   In slope-area plots (Fig. 8b) study area GC4 has a flatter profile than study areas

717   GC1, GC2 and GC3. The drop in slope at high drainage areas in GC4 is probably an artefact

718 of the low number of pixels included in the slope calculations in the last 5 to 10 points. In the

719 CAD plot (Fig. 9b), study area GC4 has a similar shape to talus systems on Earth (Fig. 7a).

720 The talus interpretation for GC4 is supported by additional evidence: (1) there is no evidence

721 for channels (Fig. 4e), (2) the wetness index plot (Fig. 11e) is similar to talus slopes on Earth

722 and (3) part of the slope-area curve lies on the threshold for dry mass wasting (Fig. 8b). The

723 dip of the slope-area curve away from the threshold for dry mass wasting suggests that

724 another process with a lower slope threshold is acting, either without having an effect on the

725 CAD plot, or with the same CAD plot as talus. We hypothesise that this may be the same

726 unknown process as noted in study area PC1.

727   The combined evidence suggests that the pole and east facing slopes of the crater

728 have been affected by debris flow processes and the equator-facing slope by mass wasting

729 and an unknown process.

730 *Site KC – crater inside Kaiser Crater in Noachis Terra*

731 Our ungullied study area (KC4) shows patterns in slope-area (Fig. 8c) and CAD plots (Fig.

732 9c) very similar to the synthetic crater and creep slopes on Earth. The difference between this

733 study area and the gullied study areas (KC1 to KC3) is presumably a result of the process of

734 gully formation. Study areas KC1 to KC3 do not have slope-area plots (Fig. 8c) that fit easily

735 within the framework established so far. However, if we refer to the modelling work of

736 Tucker & Bras (1998) then the patterns in slope-area plots can be explained. At small

737 drainage areas our curves for study areas with gullies have a horizontal or slightly positive

738 trend compared to our ungullied study area, which has a definite positive trend. This suggests

739 the weak influence of diffusive processes (which generate a positive relationship in slope-

740 area plots) combined with slope threshold processes (which tend to produce horizontal

741 trends). As all the data are below the dry mass wasting threshold, this threshold process is

742 likely to be a pore pressure triggered process, such as debris flow. At intermediate drainage

743   areas there is a transitional region which occurs at a similar drainage area to the slope-

744   turnover in the ungullied section. At high drainage areas the gullied study areas show a

745   slightly decreasing sub-horizontal trend, as opposed to the ungullied study area which has a

746   well defined decrease in slope with drainage area. This also can be attributed to a pore

747   pressure triggered threshold process but at a lower slope threshold than the previous process.

748   In CAD plots (Fig. 9c) study areas KC1 to KC3 are consistent with debris flow processes.

749   The wetness index plots for these study areas (Fig. 11f) are similar to terrestrial debris flow

750   study areas which have been influenced by alluvial processes (e.g., site WF, Figs. 10g and

751   10h). This suggests that the first pore pressure threshold in slope-area plots is due to debris

752   flow and the second lower one due to an unknown process, which again could be the same

753   process affecting sites PC and GC.

754   In slope-area plots, the gully heads on this slope (Fig. 8c) coincide with the drainage

755   area of the slope turnover in study area KC4 and the transitional study areas of KC1 to KC3.

756   This coincident relationship matches the observations made by many authors who have

757   studied gullies on Earth (e.g., Hancock & Evans 2006). Our channel heads lie mainly in the

758   domain attributed to "pore pressure landsliding channel initiation" processes, but some also

759   lie in the "unchanneled" domain (McNamara *et al.* 2006). Notably the gully heads occur

760   below the dry mass wasting threshold, again suggesting that these martian gullies are initiated

761   by a pore pressure threshold process. The gully heads occur on slope gradients of 0.55 similar

762   to those described by Lanza *et al.* (2010), but at drainage areas an order of magnitude lower.

763   This is possibly due to the different approach used by Lanza *et al.* (2010) to measure the

764   contributing area, and possible differences in their interpretation of the location of channel

765   initiation. The co-occurrence of the gully heads with the slope-turnover in slope-area plots

766   suggests that the gullies are a result of whole-slope drainage, as previously found by Lanza *et*

767   *al.* (2010), either at the surface or shallow subsurface. Our work provides additional evidence

768　to support the conclusions of Lanza *et al.* (2010) that these gullies originate from a distributed

769　source and hence supports the surface melting model for martian gully formation, rather than

770　an aquifer source model. Further, this observation provides additional evidence that a

771　threshold process, probably debris flow, is forming these gullies, as previously suggested by

772　Lanza *et al.* (2010).

773　　　　From the combination of the slope-area, CAD and wetness index plots we infer that

774　the gullies in this crater are produced by debris flow and were initiated by surface, or near

775　subsurface, flow of water. Creep and an unknown process were likely to have been the

776　dominant processes on the ungullied crater slopes. This is consistent with the setting of these

777　gullies within the ice-rich mantle deposits which is likely to be susceptible to melting,

778　providing a distributed source of water for the gullies.

779　*Site TS – crater in Terra Sirenum*

780　Unlike the other areas we have studied on Mars, parts of the slope-area data for study area

781　TS1 at lower drainage areas (Fig. 8d) are above the threshold slope for dry mass wasting.

782　This is an indication that rock strength limited dry mass wasting is occurring in the upper

783　parts of the slope. In CAD plots (Fig. 9d) this study area has the classic shape of a talus or

784　creep slope. However, the slope-area trend shown by study area TS1 is very different from

785　that of the synthetic crater (Fig. 8d), which we assume to have been similar to the starting

786　point for study area TS1. This assumption carries the implication that the slope in study area

787　TS1 has evolved over time from concave to linear in profile. Study area TS1 shows a very

788　similar trend in slope-area plots as study area GC4 (Fig. 8b), but originates above the 0.7

789　slope threshold. As discussed previously for study area GC4, in the framework of Tucker &

790　Bras (1998) such a pattern is likely to reflect a gradual transition from the dominance of a dry

791　mass wasting threshold at lower drainage areas to the dominance of a pore pressure triggered

792　slope threshold due to an unknown process at higher drainage areas. However, in the case of

793   TS1 this signal not only includes dry mass wasting of non-cohesive material, but rockwall

794   mass wasting as well. The wetness index map shows that the slope does not concentrate

795   drainage, except for some diffuse linear areas, again resembling talus slopes on Earth. The

796   combination of the slope-area plot, CAD plot and wetness index map suggests a dominantly

797   dry mass wasting evolution of this slope, which fits well with the visual observations.

798   *Solifluction on slopes on Mars*

799   In many of the Mars study sites we have inferred an unknown process that is

800   responsible for a second, lower-slope pore pressure triggered threshold in the slope-area

801   plots. However, this process seems to produce slopes that yield a CAD plot that is similar to

802   talus on Earth, i.e. it does not concentrate drainage. As suggested by Tucker & Bras (1998)

803   another threshold process which would produce a similar response in slope-area plots to pore

804   pressure induced landsliding is solifluction. Solifluction in frozen landscapes comprises the

805   combined action of gelifluction and frost creep, and describes the slow, down slope

806   movement of water saturated debris or soils. Solifluction requires freezing and thawing to

807   generate elevated pore pressures and occurs at lower slope angles than pore pressure induced

808   failure, which can trigger landslides and debris flow (Harris *et al.* 2008). This process is

809   consistent with the recent observations of periglacial landform assemblages on Mars (Balme

810   & Gallagher 2009; Balme *et al.* 2009; Soare & Osinski 2009).

811   **Implications for the formation process of martian gullies**

812   Dietrich & Perron (2006) suggested that the lack of biotic processes on Mars would promote

813   erosion by rilling and gullying and stripping of the fine surface materials, given a suitable

814   water source. This would lead to a slope-area plot that lacked a distinct slope turnover,

815   similar to the slope-area plots seen in the Death Valley data (our site DV – Fig. 6d).

816   However, inspecting the trends in the slope-area plots for the Mars systems in Fig. 8, one of

817   the most apparent differences from Earth is the presence of this slope turnover. This indicates

818   that creep is a more dominant process on martian hillslopes than on those we studied on

819   Earth; contradictory to the predictions made by Dietrich & Perron (2006). The creep signal

820   in most published slope-area plots on Earth is induced predominantly by biota, hence on

821   Mars the creep must be facilitated using a different mechanism. Perron *et al.* (2003) observed

822   using Mars Orbiter Laser Altimeter (MOLA) data that slopes on Mars have average gradients

823   well below 35° and suggested that ice driven creep is the cause. Other potential creep

824   mechanisms include frost heave and shrink-swell in clays and hydrated salts, both of which

825   produce creep on un-vegetated and un-bioturbated slopes on Earth. These mechanisms

826   however would require widespread and relatively large amounts of liquid water, which is

827   considered unlikely under current or geologically recent martian climate. Hence, we believe

828   that ice driven creep provides the best explanation for the signals seen in our slope-area data

829   from Mars. In accordance with their results, most of the slopes we studied on Mars also have

830   average gradients well below 35°, with the exception of slope TS1, whose average gradients

831   are partially above 35°.

832   Virtually every gully that we have studied on Mars has the distinct signal of debris

833   flow as the dominant gully forming process. Lanza *et al.* (2010) also found visual and

834   morphometric evidence of debris flows in these areas. The notable exception is area PC1, the

835   slope containing the new light-toned deposits. However, this area does not include gullies of

836   a normal form (Fig. 1) as they lack well defined alcoves and channels. Examination of a far

837   greater number of DEMs containing gullies would be needed to confirm debris flow as the

838   main gully forming process on Mars. However, if this is the principal mechanism, brings up

839   the following hypotheses and predictions for the formation of gullies on Mars:

840   (1)   The high sediment concentrations and low infiltration rates could protect the water

841   from evaporation.

842   (2)   The energy released by grain interactions within the flow could retard freezing.

843   (3)   Basal freezing (Conway *et al.* 2010a) or a permafrost layer could facilitate the

844   saturation of the sediment that is required to generate the high pore water pressures

845   to trigger debris flow.

846   (4)   Expected depositional features include levées and lobes.

847   (5)   Expected erosional features include discrete slip scars.

848   Points 1-3 of are hard to observe or test, but the erosional and depositional features

849   can be detected in the high resolution HiRISE images. Failure scars have been noted by other

850   authors (Dickson & Head 2009) from HiRISE images and are present within our study areas.

851   Depositional lobes have also been noted by other authors (Levy *et al.* 2009; Lanza *et al.*

852   2010). Visual observations have been made of debris flow levées (Lanza *et al.* 2010), but

853   DEMs from HiRISE are not yet of sufficient quality to reliably resolve debris flow levées.

854   High quality DEMs would allow the estimation of individual flow volumes (Conway *et al.*

855   2010b), which could be used to constrain models of gully formation. This should be a priority

856   for future work, as it would allow more accurate estimates of the amounts of water associated

857   with formation of gully landforms.

858   A debris flow, once triggered, results in more erosion and deposition with less water

859   than pure water flow. This means that high discharges, invoked by other workers (Heldmann

860   *et al.* 2005; Hart *et al.* 2009), are not required to form martian gullies. Modelling has shown

861   that surface melting produces only small amounts of liquid water (Williams *et al.* 2009). This

862   has been one of the major criticisms of the surface melting model. However, if gullies are

863   formed mainly by debris flow, points (1) and (2) above indicate that relatively small amounts

864   of water are needed.

Implications for the water source of martian gullies

The observed relationship in slope-area plots between the slope turnover and the location of gully heads in site KC on Mars is an important observation and indicates that the transition from concave to convex topography is closely linked to gully formation. This would not be expected in an aquifer system, as channel formation would be controlled predominantly by the location of aquifer bodies rather than the shape of the landscape (Fetter 2001). Our work indicates that a widely distributed source of surface or shallow subsurface flow in site KC would be the most satisfactory explanation, in support of the conclusions of Lanza *et al.* (2010). Because our data do not show a definite trend in slope-area plots this indicates that the channels originate from shallow sub-surface flow (Hattanji *et al.* 2006; Jaeger *et al.* 2007; Imaizumi *et al.* 2010), or more likely surface flow in a soil poor landscape (Larsen *et al.* 2006). A potential source for this near surface water is the mantle deposits, which have been observed on both this slope and in site PC2 and has been linked to gully formation by other authors (Christensen 2003; Aston *et al.* 2010; van Gasselt *et al.* 2010).

The development of equally spaced incised alcoves in site GC can either be attributed to geological controls (e.g., faulting), or landscape self organisation from an interlinked debris flow-alluvial system (Perron *et al.* 2009). We argue against a structural control, because there is a lack of these organised alcoves on the equator-facing slope. Hence, considering that we conclude debris flow to be the dominant gully forming process on this crater slope, it would seem most likely that these self-organised alcoves are a result of this process. This kind of self organisation requires a landscape that responds to a distributed water source as on Earth rather than an aquifer source.

Kreslavsky & Head (2003) and Kreslavsky *et al.* (2008) found that pole-facing slopes between 40-50° latitude in both hemispheres were systematically gentler than equator-facing slopes. They suggest that this is due to insolation asymmetry and melting of ice on

890 pole-facing slopes during periods of high obliquity, similar to the model proposed by Costard

891 *et al.* (2002) for gully formation on pole-facing slopes. Our study sites also show this

892 asymmetry: pole-facing slopes are longer and have a greater variety of slope angles and are

893 more concave, whereas the equator-facing slopes are shorter and have a more uniform

894 distribution of slopes and are more linear. There is a marked difference in geomorphological

895 process between crater walls with different aspects in the two craters that we studied (sites

896 PC and GC). The observed asymmetry of process and form supports the model of a climatic

897 influence on gully formation and general slope development of the craters. However, many

898 more sites would have to be studied to verify this for gullies in general.

Conclusions

900 We have shown the potential of applying quantitative geomorphological analysis techniques

901 commonly used on Earth for discriminating between different active processes on Mars.

902 Specifically we have validated the use of slope-area plots, cumulative area distribution

903 (CAD) plots, and wetness index maps on small slope sections of less than one square

904 kilometre. We have shown that pure water (alluvial) flow, debris flow and dry mass wasting

905 dominated slopes can be satisfactory discriminated on Earth. By applying these techniques to

906 four areas of Mars containing recent gullies we have inferred that debris flow is the dominant

907 gully forming process. However, we have also inferred that, as on Earth, gully formation on

908 Mars is a complex process: slopes on Mars are likely to have been affected by a variety of

909 processes that lead to a mixture of signals from our geomorphological analyses. Despite this,

910 we have not found the distinctive geomorphological fingerprint of pure water flow on slopes

911 that host gullies. Its absence, however, does not prove the absence of the process. Our results

912 are consistent with the possibility that ice driven creep and solifluction are, or have recently

913 been, active in modifying crater slopes on Mars.

914	From the location of gully heads within the landscape, and by studying the form of

915	alcoves, it is apparent that at least two of the sites examined contain gullies which have been

916	formed from a widely distributed source of water. This is most easily explained by a surface

917	melting source for the water. The model of Costard *et al.* (2002) provides a mechanism by

918	which the cause of this melting was increased insolation during past high obliquity

919	excursions. Our preliminary observations of an asymmetry in process and form around the

920	impact craters provides additional support for this model, but we cannot rule out surface

921	melting at present day, or during other epochs.

922	Our geomorphological evidence for debris flow as an active process in forming

923	gullies is reinforced by visual observations. Debris flow as a process leaves distinct

924	geomorphological features, such as failure scars and lobate deposits, which have been

925	observed both here and in previous studies (Dickson & Head 2009; Levy *et al.* 2009; Lanza

926	*et al.* 2010). Unfortunately the topographic data on Mars are not yet sufficient for the

927	discrimination of these features and flanking levées in DEMs, which would allow accurate

928	estimation of individual flow volumes and thus estimation of the volumes of water needed to

929	form the gullies (Conway *et al.* 2010b).

930	**Appendix 1**

931	The derivation of the shear stress erosion model relies on the assumption that erosion rate (E)

932	is a power law of bed shear stress (τ_b):

933

934	$$E = k\,\tau_b^{\ a} \tag{2}$$

935

936   where k and a are positive constants. Following Snyder (2000), Whipple & Tucker

937   (1999) we use the assumptions of conservation of mass (water) and steady uniform flow to

938   obtain the following expression of basal shear stress:

939

940
$$\tau_b = \rho C_f^{1/3}\left(\frac{gSQ}{W}\right)^{2/3} \tag{3}$$

941

942   where ρ is the density of water, C_f is a dimensionless friction factor, g is the acceleration due

943   to gravity, S is the local channel slope, Q is the stream discharge and W is the stream width.

944   We then include a relationship for basin hydrology and hydraulic geometry given by:

945

946
$$Q = k_q A^c \tag{4}$$

947
$$W = k_w Q^b \tag{5}$$

948

949   where k_q and k_w are constants, A is the drainage area and b and c are positive dimensionless

950   constants. Combining 2-5, leads to:

951

952
$$E = k_e A^m S^n \tag{6}$$

953

954   where:

955

956
$$k_e = k_b k_w^{-2a/3} k_q^{2a(1-b)/3} \rho^a g^{2a/3} \tag{7}$$

957
$$m = (2ac/3)(1\text{-}b) \tag{8}$$

958
$$n = 2a/3 \tag{9}$$

959

960   Given this, if we now define a constant k_m for Mars, based on the assumption that gravitation

961   acceleration is approximately one third that on Earth:

962

$$k_m = (1/3)^{2a/3} k_e = (1/3)^n k_e \tag{7}$$

963

964

965   To derive (1), in the main text, we have to include the expectation that over long timescales,

966   uplift rate (U) and erosion rate compete to change the landscape elevation (z):

967

$$\frac{\partial z}{\partial t} = U - E = U - k_e A^m S^n \tag{8}$$

968

969

970   where t is a given time-step. Now if we assume that the system is in equilibrium in which

971   erosion is balanced by uplift rate, $\partial z/\partial t = 0$, then:

972

$$S = (U/k_e)^{1/n} A^{-m/n} \tag{9}$$

973

974

975   Comparing this to equation (1), in the main text, we have:

976

$$k = (U/k_e)^{1/n} \tag{10}$$

977

$$\theta = -m/n \tag{11}$$

978

979

980   If we then include our k_m constant (7) for Mars in (9) we get:

981

$$S = (U/k_m)^{1/n} A^{-m/n} \tag{12}$$

982

$$S = 3(U/k_e)^{1/n} A^{-m/n} \tag{13}$$

983

984

985   Thus for a given drainage area on Earth we would expect the slope on Mars to be three times

986   smaller. Or, in log-log terms:

987

988                               $Log\ S = log3 + 1/n\ log(U/ke) - m/n\ logA$ (14)

989

1001

References

Akca, D. 2007a. *Least Squares 3D Surface Matching*. PhD thesis, Eidgenössische Technische Hochschule, Zürich.

Akca, D. 2007b. Matching of 3D surfaces and their intensities. *ISPRS Journal of Photogrammetry and Remote Sensing*, **62**, 2, 112-121.

Aston, A. H., Conway, S. J. & Balme, M. R. 2010. Identifying Martian gully evolution. *In:* Balme, M., Bargery, A. S., Gallagher, C. & Gupta, S. (eds), *Geomorphology on Mars and Other Planets*. The Geological Society of London, accepted.

Balme, M., Mangold, N., Baratoux, D., Costard, F., Gosselin, M., Masson, P., Pinet, P. & Neukum, G. 2006. Orientation and distribution of recent gullies in the southern hemisphere of mars: Observations from High Resolution Stereo Camera/Mars Express (HRSC/MEX) and Mars Orbiter Camera/Mars Global Surveyor (MOC/MGS) data. *Journal of Geophysical Research - Planets; *, **111**, E5, doi:10.1029/2005JE002607

Balme, M. R. & Gallagher, C. 2009. An equatorial periglacial landscape on Mars. *Earth and Planetary Science Letters*, **285**, 1-2, 1-15.

Balme, M. R., Gallagher, C. J., Page, D. P., Murray, J. B. & Muller, J. P. 2009. Sorted stone circles in Elysium Planitia, Mars: Implications for recent martian climate. *Icarus*, **200**, 1, 30-38.

Ben David-Novak, H., Morin, E. & Enzel, Y. 2004. Modern extreme storms and the rainfall thresholds for initiating debris flows on the hyperarid western escarpment of the Dead Sea, Israel. *Geological Society of America Bulletin*, **116**, 5-6, 718-728.

Blair, T. C. 1999. Cause of dominance by sheetflood vs. debris-flow processes on two adjoining alluvial fans, Death Valley, California. *Sedimentology*, **46**, 6, 1015-1028.

Blair, T. C. 2000. Sedimentology and progressive tectonic unconformities of the sheetflood-dominated Hell's Gate alluvial fan, Death Valley, California. *Sedimentary Geology*, **132**, 3-4, 233-262.

Borga, M., Tonelli, F. & Selleroni, J. 2004. A physically based model of the effects of forest roads on slope stability. *Water Resources Research*, **40**, 12, 1-9.

Bourke, M. C. 2005. Alluvial Fans on Dunes in Kaiser Crater Suggest Niveo-Aeolian and Denivation Processes on Mars. *Lunar and Planetary Science Conference*, **36**, no. 2373.

Brardinoni, F. & Hassan, M. A. 2006. Glacial erosion, evolution of river long profiles, and the organization of process domains in mountain drainage basins of coastal British Columbia. *Journal of Geophysical Research - Earth Surface*, **111**, 1, doi:10.1029/2005JF000358.

Brook, M. S., Kirkbride, M. P. & Brock, B. W. 2008. Temporal constraints on glacial valley cross-profile evolution: Two Thumb Range, central Southern Alps, New Zealand. *Geomorphology*, **97**, 1-2, 24-34.

Chandler, R. J. 1973. The Inclination of Talus, Artic Talus terraces, and Other Slopes Composed of Granular Materials. *Journal of Geology*, **81**, 1-14.

Chevrier, V. & Altheide, T. S. 2008. Low temperature aqueous ferric sulfate solutions on the surface of Mars. *Geophysical Research Letters*, **35**, L22101, L22101

Christensen, P. R. 2003. Formation of recent martian gullies through melting of extensive water-rich snow deposits. *Nature*, **422**, 6927, 45-48.

1048 Coe, J. A., Godt, J. W. & Henceroth, A. J. 2002. *Debris Flows along the Interstate 70*
1049   *Corridor, Floyd Hill to the Arapahoe Basin Ski Area, Central Colorado – A Field*
1050   *Trip Guidebook*. U.S. Geological Survey Open-File Report, USGS, Open-File Report
1051   02-398.
1052 Conway, S. J., Balme, M. R., Lamb, M. P., Towner, M. C. & Murray, J. B. 2010a. Enhanced
1053   runout and erosion by overland flow under subfreezing and low pressure conditions:
1054   experiments and application to Mars. *Icarus*, **in review**.
1055 Conway, S. J., Decaulne, A., Balme, M. R., Murray, J. B. & Towner, M. C. 2010b. A new
1056   Approach to Estimating Hazard posed by Debris Flows in the Westfjords of Iceland.
1057   *Geomorphology*, **114**, 4, 556-572.
1058 Costard, F., Forget, F., Mangold, N. & Peulvast, J. P. 2002. Formation of recent Martian
1059   debris flows by melting of near-surface ground ice at high obliquity. *Science*, **295**,
1060   5552, 110-113.
1061 Crippen, J. R. 1979. *Potential hazards from floodflows and debris movement in the Furnace*
1062   *Creek area, Death Valley National Monument, California-Nevada*. U.S. Geological
1063   Survey Open-File Report, **79-991**, USGS.
1064 Crosta, G. B. & Frattini, P. 2008. Rainfall-induced landslides and debris flows. *Hydrological*
1065   *Processes*, **22**, 4, 473-477.
1066 Decaulne, A., Sæmundsson & Pétursson, O. 2005. Debris flow triggered by rapid snowmelt:
1067   A case study in the Gleiðarhjalli area, northwestern Iceland. *Geografiska Annaler.*
1068   *Series A, Physical Geography*, **87A**, 4, 487-500.
1069 Decaulne, A. & Sæmundsson 2007. Spatial and temporal diversity for debris-flow
1070   meteorological control in subarctic oceanic periglacial environments in Iceland. *Earth*
1071   *Surface Processes and Landforms*, **32**, 1971-1983.
1072 Dickson, J. L., Head, J. W. & Kreslavsky, M. 2007. Martian gullies in the southern mid-
1073   latitudes of Mars: Evidence for climate-controlled formation of young fluvial features
1074   based upon local and global topography. *Icarus*, **188**, 315-323.
1075 Dickson, J. L. & Head, J. W. 2009. The formation and evolution of youthful gullies on Mars:
1076   Gullies as the late-stage phase of Mars' most recent ice age. *Icarus*, **204**, 1, 63-86.
1077 Dietrich, W. E. & Perron, J. T. 2006. The search for a topographic signature of life. *Nature*,
1078   **439**, 7075, 411-418.
1079 Fetter, C. W., 2001. *Applied Hydrogeology*. Prentice Hall, New Jersey, 598 pp.
1080 Gaidos, E. J. 2001. Cryovolcanism and the recent flow of liquid water on Mars. *Icarus*, **153**,
1081   1, 218-223.
1082 Garvin, J. B., Sakimoto, S. E. H., Schnetzler, C. & Frawley, J. J. 1999. Global Geometric
1083   Properties of Martian Impact Craters: A Preliminary Assessment Using Mars Orbiter
1084   Laser Altimeter (MOLA). *The Fifth International Conference on Mars, July 19-24,*
1085   *1999, Pasadena, California*, abstract no.6163.
1086 Godt, J. W. & Coe, J. A. 2007. Alpine debris flows triggered by a 28 July 1999 thunderstorm
1087   in the central Front Range, Colorado. *Geomorphology*, **84**, 1-2, 80-97.
1088 Hack, J. T. 1957. Studies of longitudinal stream profiles in Virginia and Maryland. *U.S.*
1089   *Geological Survey Professional Paper*, **294-B**, 45-97.
1090 Hancock, G. R. & Evans, K. G. 2006. Channel head location and characteristics using digital
1091   elevation models. *Earth Surface Processes and Landforms*, **31**, 7, 809-824.
1092 Harris, C., Smith, J. S., Davies, M. C. R. & Rea, B. 2008. An investigation of periglacial
1093   slope stability in relation to soil properties based on physical modelling in the
1094   geotechnical centrifuge. *Geomorphology*, **93**, 3-4, 437-459.
1095 Harris, S. A. & Gustafson, C. A. 1993. Debris flow characteristics in an area of continuous
1096   permafrost, St. Elias Range, Yukon Territory. *Zeitschrift für Geomorphologie,*, **37**, 1,
1097   41-56.

1098 Hart, S. D., Gulick, V. C., Parsons, R. A. & Barnhart, C. J. 2009. Gully Slopes and
1099   Discharges on Lyot Crater's Central Peak. *Lunar and Planetary Science Conference*,
1100   **40**, no. 2349.
1101 Hattanji, T., Onda, Y. & Matsukura, Y. 2006. Thresholds for bed load transport and channel
1102   initiation in a chert area in Ashio Mountains, Japan: An empirical approach from
1103   hydrogeomorphic observations. *Journal of Geophysical Research - Earth Surface*,
1104   **111**, 2, doi:10.1029/2004JF000206.
1105 Hecht, M. H. 2002. Metastability of liquid water on Mars. *Icarus*, **156**, 2, 373-386.
1106 Heldmann, J. L. & Mellon, M. T. 2004. Observations of martian gullies and constraints on
1107   potential formation mechanisms. *Icarus*, **168**, 2, 285-304.
1108 Heldmann, J. L., Toon, O. B., Pollard, W. H., Mellon, M. T., Pitlick, J., McKay, C. P. &
1109   Andersen, D. T. 2005. Formation of Martian gullies by the action of liquid water
1110   flowing under current Martian environmental conditions. *Journal of Geophysical*
1111   *Research - Planets*, **110**, E5, doi:10.1029/2004JE002261.
1112 Heldmann, J. L., Carlsson, E., Johansson, H., Mellon, M. T. & Toon, O. B. 2007.
1113   Observations of martian gullies and constraints on potential formation mechanisms II.
1114   The northern hemisphere. *Icarus*, **188**, 324-344.
1115 Heldmann, J. L., Conley, C., Brown, A. J., Fletcher, L., Bishop, J. L. & McKay, C. P. 2010.
1116   Possible Liquid Water Origin for Atacama Desert Mudflow and Recent Gully
1117   Deposits on Mars. *Icarus*, **206**, 2, 685-690.
1118 Imaizumi, F., Hattanji, T. & Hayakawa, Y. S. 2010. Channel initiation by surface and
1119   subsurface flows in a steep catchment of the Akaishi Mountains, Japan.
1120   *Geomorphology*, **115**, 1-2, 32-42.
1121 Innes, J. L. 1983. Debris Flows. *Progress in Physical Geography*, **7**, 469-501.
1122 Iverson, R. M. 1997. The physics of debris flows. *Reviews of Geophysics*, **35**, 3, 245-296.
1123 Jack, J. L. 2000. Red-shifts and red herrings in geographical ecology. *Ecography*, **23**, 1, 101-
1124   113.
1125 Jaeger, K. L., Montgomery, D. R. & Bolton, S. M. 2007. Channel and perennial flow
1126   initiation in headwater streams: Management implications of variability in source-area
1127   size. *Environmental Management*, **40**, 5, 775-786.
1128 Kirk, R. L., Howington-Kraus, E., Rosiek, M. R., Anderson, J. A., Archinal, B. A., Becker,
1129   K. J., Cook, D. A., Galuszka, D. M., Geissler, P. E., Hare, T. M., Holmberg, I. M.,
1130   Keszthelyi, L. P., Redding, B. L., Delamere, W. A., Gallagher, D., Chapel, J. D.,
1131   Eliason, E. M., King, R. & McEwen, A. S. 2008. Ultrahigh resolution topographic
1132   mapping of Mars with MRO HiRISE stereo images: Meter-scale slopes of candidate
1133   Phoenix landing sites. *Journal of Geophysical Research - Planets*, **113**,
1134   doi:10.1029/2007JE003000.
1135 Kirkby, M. J., Bull, L. J., Poesen, J., Nachtergaele, J. & Vandekerckhove, L. 2003. Observed
1136   and modelled distributions of channel and gully heads - with examples from SE Spain
1137   and Belgium. *Catena*, **50**, 2-4, 415-434.
1138 Kneissl, T., Reiss, D., van Gasselt, S. & Neukum, G. 2009. Distribution and orientation of
1139   northern-hemisphere gullies on Mars from the evaluation of HRSC and MOC-NA
1140   data. *Earth and Planetary Science Letters*, **In Press, Corrected Proof**.
1141 Kobor, J. S. & Roering, J. J. 2004. Systematic variation of bedrock channel gradients in the
1142   central Oregon Coast Range: Implications for rock uplift and shallow landsliding.
1143   *Geomorphology*, **62**, 3-4, 239-256.
1144 Kolb, K. J., Pelletier, J. D. & McEwen, A. S. 2010. Modeling the formation of bright slope
1145   deposits associated with gullies in Hale Crater, Mars: Implications for recent liquid
1146   water. *Icarus*, **205**, 1, 113-137.

1147 Kreslavsky, M. A. & Head, J. W. 2003. North-south topographic slope asymmetry on Mars:
1148   Evidence for insolation-related erosion at high obliquity. *Geophysical Research*
1149   *Letters*, **30**, 15, doi:10.1029/2003GL017795.
1150 Kreslavsky, M. A., Head, J. W. & Marchant, D. R. 2008. Periods of active permafrost layer
1151   formation during the geological history of Mars: Implications for circum-polar and
1152   mid-latitude surface processes. *Planetary and Space Science*, **56**, 2, 289-302.
1153 Lague, D. & Davy, P. 2003. Constraints on the long-term colluvial erosion law by analyzing
1154   slope-area relationships at various uplift rates in the Siwaliks Hills (Nepal). *Journal of*
1155   *Geophysical Research - Solid Earth*, **108**, 2, doi:10.1029/2002JB001893.
1156 Lanza, N. L., Meyer, G. A., Okubo, C. H., Newsom, H. E. & Wiens, R. C. 2010. Evidence
1157   for debris flow gully formation initiated by shallow subsurface water on Mars. *Icarus*,
1158   **205**, 1, 103-112.
1159 Larsen, I. J., Pederson, J. L. & Schmidt, J. C. 2006. Geologic versus wildfire controls on
1160   hillslope processes and debris flow initiation in the Green River canyons of Dinosaur
1161   National Monument. *Geomorphology*, **81**, 1-2, 114-127.
1162 Levy, J. S., Head, J. W., Dickson, J. L., Fassett, C. I., Morgan, G. A. & Schon, S. C. 2009.
1163   Identification of gully debris flow deposits in Protonilus Mensae, Mars:
1164   Characterization of a water-bearing, energetic gully-forming process. *Earth and*
1165   *Planetary Science Letters*, **In Press, Corrected Proof**.
1166 Malin, M. C. & Edgett, K. S. 2000. Evidence for recent groundwater seepage and surface
1167   runoff on Mars. *Science*, **288**, 5475, 2330-2335.
1168 Malin, M. C., Edgett, K. S., Posiolova, L. V., McColley, S. M. & Dobrea, E. Z. N. 2006.
1169   Present-day impact cratering rate and contemporary gully activity on Mars. *Science*,
1170   **314**, 5805, 1573-1577.
1171 Mangeney, A., Bouchut, F., Thomas, N., Vilotte, J. P. & Bristeau, M. O. 2007. Numerical
1172   modeling of self-channeling granular flows and of their levee-channel deposits.
1173   *Journal of Geophysical Research - Earth Surface*, **112**, 2, doi:10.1029/2006JF000469.
1174 Mangold, N. 2005. High latitude patterned grounds on Mars: Classification, distribution and
1175   climatic control. *Icarus*, **174**, 336-359.
1176 Mao, L., Cavalli, M., Comiti, F., Marchi, L., Lenzi, M. A. & Arattano, M. 2009. Sediment
1177   transfer processes in two Alpine catchments of contrasting morphological settings.
1178   *Journal of Hydrology*, **364**, 1-2, 88-98.
1179 Marchi, L., Dalla Fontana, G., Cavalli, M. & Tagliavini, F. 2008. Rocky headwaters in the
1180   Dolomites, Italy: Field observations and topographic analysis. *Arctic Antarctic and*
1181   *Alpine Research*, **40**, 4, 685-694.
1182 McEwen, A. S., Hansen, C. J., Delamere, W. A., Eliason, E. M., Herkenhoff, K. E.,
1183   Keszthelyi, L., Gulick, V. C., Kirk, R. L., Mellon, M. T., Grant, J. A., Thomas, N.,
1184   Weitz, C. M., Squyres, S. W., Bridges, N. T., Murchie, S. L., Seelos, F., Seelos, K.,
1185   Okubo, C. H., Milazzo, M. P., Tornabene, L. L., Jaeger, W. L., Byrne, S., Russell, P.
1186   S., Griffes, J. L., MartÃnez-Alonso, S., Davatzes, A., Chuang, F. C., Thomson, B. J.,
1187   Fishbaugh, K. E., Dundas, C. M., Kolb, K. J., Banks, M. E. & Wray, J. J. 2007. A
1188   closer look at water-related geologic activity on Mars. *Science*, **317**, 5845, 1706-1709.
1189 McNamara, J. P., Ziegler, A. D., Wood, S. H. & Vogler, J. B. 2006. Channel head locations
1190   with respect to geomorphologic thresholds derived from a digital elevation model: A
1191   case study in northern Thailand. *Forest Ecology and Management*, **224**, 1-2, 147-156.
1192 Miller, D. J. 1961. *Geology of the Katalla district, Gulf of Alaska Tertiary province, Alaska*.
1193   U.S. Geological Survey Open-File Report.
1194 Montgomery, D. R. & Foufoula-Georgiou, E. 1993. Channel network source representation
1195   using digital elevation models. *Water Resources Research*, **29**, 12, 3925-3934.

1196   Moore, H. J. & Jakosky, B. M. 1989. Viking landing sites, remote-sensing observations, and
1197   physical properties of Martian surface materials. *Icarus*, **81**, 164-184.
1198   Morton, D. M., Alvarez, R. M., Ruppert, K. R. & Goforth, B. 2008. Contrasting rainfall
1199   generated debris flows from adjacent watersheds at Forest Falls, southern California,
1200   USA. *Geomorphology*, **96**, 3-4, 322-338.
1201   Moyle, W. R. 1982. *Water Resources of Borrego Valley and Vicinity, California: Phase 1 -*
1202   *Definition of Geologic and Hydrologic Characteristics of a Basin*. U.S. Geological
1203   Survey Open-File Report, **82-855**, USGS.
1204   Musselwhite, D. S., Swindle, T. D. & Lunine, J. I. 2001. Liquid CO_2 breakout and the
1205   formation of recent small gullies on Mars. *Geophysical Research Letters*, **28**, 7, 1283-
1206   1285.
1207   Mustard, J. F., Cooper, C. D. & Rifkin, M. K. 2001. Evidence for recent climate change on
1208   Mars from the identification of youthful near-surface ground ice. *Nature*, **412**, 6845,
1209   411-414.
1210   Norðdalh, H. 1990. Late Weichselian and early Holocene deglaciation history of Iceland.
1211   *Jökull*, **40**, 27-50.
1212   Pelletier, J. D., Kolb, K. J., McEwen, A. S. & Kirk, R. L. 2008. Recent bright gully deposits
1213   on Mars: Wet or dry flow? *Geology*, **36**, 3, 211-214.
1214   Perera, H. & Willgoose, G. 1998. A physical explanation of the cumulative area distribution
1215   curve. *Water Resources Research*, **34**, 5, 1335-1343.
1216   Perron, J. T., Dietrich, W. E., Howard, A. D., McKean, J. A. & Pettinga, J. R. 2003. Ice-
1217   driven creep on Martian debris slopes. *Geophysical Research Letters*, **30**, 14,
1218   doi:10.1029/2003GL017603.
1219   Perron, J. T., Kirchner, J. W. & Dietrich, W. E. 2009. Formation of evenly spaced ridges and
1220   valleys. *Nature*, **460**, 7254, 502-505.
1221   Peters, G. H., Abbey, W., Bearman, G. H., Mungas, G. S., Smith, J. A., Anderson, R. C.,
1222   Douglas, S. & Beegle, L. W. 2008. Mojave Mars simulant--Characterization of a new
1223   geologic Mars analog. *Icarus*, **197**, 2, 470-479.
1224   Reiss, D., van Gasselt, S., Neukum, G. & Jaumann, R. 2004. Absolute dune ages and
1225   implications for the time of formation of gullies in Nirgal Vallis, Mars. *Journal of*
1226   *Geophysical Research - Planets*, **109**, E6, doi:10.1029/2004JE002251.
1227   Schon, S. C., Head, J. W. & Fassett, C. I. 2009. Unique chronostratigraphic marker in
1228   depositional fan stratigraphy on Mars: Evidence for ca. 1.25 Ma gully activity and
1229   surficial meltwater origin. *Geology*, **37**, 3, 207-210.
1230   Selby, M. J., 1993. *Hillslope Materials and Processes*. Oxford University Press, Oxford, 451
1231   pp.
1232   Shinbrot, T., Duong, N. H., Kwan, L. & Alvarez, M. M. 2004. Dry granular flows can
1233   generate surface features resembling those seen in Martian gullies. *Proceedings of the*
1234   *National Academy of Sciences of the United States of America*, **101**, 23, 8542-8546.
1235   Sirkin, L. & Tuthill, S. J. 1987. Late Pleistocene and Holocene deglaciation and
1236   environments of the southern Chugach Mountains, Alaska. *Geological Society of*
1237   *America Bulletin*, **99**, 376-384.
1238   Snyder, N. P., Whipple, K. X., Tucker, G. E. & Merritts, D. J. 2000. Landscape response to
1239   tectonic forcing: Digital elevation model analysis of stream profiles in the Mendocino
1240   triple junction region, Northern California. *Bulletin of the Geological Society of*
1241   *America*, **112**, 8, 1250-1263.
1242   Soare, R. J. & Osinski, G. R. 2009. Stratigraphical evidence of late Amazonian periglaciation
1243   and glaciation in the Astapus Colles region of Mars. *Icarus*, **202**, 17-21.
1244   Stock, J. & Dietrich, W. E. 2003. Valley incision by debris flows: Evidence of a topographic
1245   signature. *Water Resources Research*, **39**, 4, doi:10.1029/2001WR001057.

1246   Stock, J. D. & Dietrich, W. E. 2006. Erosion of steepland valleys by debris flows. *Bulletin of*
1247   *the Geological Society of America*, **118**, 9-10, 1125-1148.
1248   Tarboton, D. G., Bras, R. L. & Rodriguez-Iturbe, I. 1991. On the extraction of channel
1249   networks from digital elevation data. *Hydrological Processes*, **5**, 1, 81-100.
1250   Tarboton, D. G. 1997. A new method for the determination of flow directions and upslope
1251   areas in grid digital elevation models. *Water Resources Research*, **33**, 2, 309-319.
1252   Tarolli, P. & Fontana, G. D. 2009. Hillslope-to-valley transition morphology: New
1253   opportunities from high resolution DTMs. *Geomorphology*, **113**, 1-2, 47-56.
1254   Treiman, A. H. 2003. Geologic settings of Martian gullies: Implications for their origins.
1255   *Journal of Geophysical Research - Planets; *, **108**, E4, doi:10.1029/2002JE001900.
1256   Tucker, G. E. & Bras, R. L. 1998. Hillslope processes, drainage density, and landscape
1257   morphology. *Water Resources Research*, **34**, 10, 2751-2764.
1258   van Gasselt, S., Hauber, E., Pio Rossi, A., Dumke, A., Orosei, R. & Neukum, G. 2010.
1259   Periglaical Geomorphology of Tempe Terra, Mars: role of mantling deposits in lobate
1260   debris apron formation and evolution. *In:* Balme, M., Bargery, A. S., Gallagher, C. &
1261   Gupta, S. (eds), *Geomorphology on Mars and Other Planets*. The Geological Society
1262   of London, in review.
1263   Whipple, K. X. & Tucker, G. E. 1999. Dynamics of the stream-power river incision model:
1264   Implications for height limits of mountain ranges, landscape response timescales, and
1265   research needs. *Journal of Geophysical Research - Solid Earth*, **104**, B8, 17661-
1266   17674.
1267   Williams, K. E., Toon, O. B., Heldmann, J. L. & Mellon, M. T. 2009. Ancient melting of
1268   mid-latitude snowpacks on Mars as a water source for gullies. *Icarus*, **200**, 2, 418-
1269   425.
1270   Woods, R. A. & Sivapalan, M. 1997. A connection between topographically driven runoff
1271   generation and channel network structure. *Water Resources Research*, **33**, 12, 2939-
1272   2950.
1273   Workman, J. B., Menges, C. M., Page, W. R., Taylor, E. M., Ekren, E. B., Rowley, P. D.,
1274   Dixon, G. L., Thompson, R. A. & Wright, L. A. 2002. Geologic map of the Death
1275   Valley ground-water model area, Nevada and California, Miscellaneous Field Studies
1276   Map 2381-A. USGS.
1277   Yetemen, O., Istanbulluoglu, E. & Vivoni, E. R. 2010. The implications of geology, soils,
1278   and vegetation on landscape morphology: Inferences from semi-arid basins with
1279   complex vegetation patterns in Central New Mexico, USA. *Geomorphology*, **116**, 3-4,
1280   246-263.
1281
1282
1283

Figure Captions

Fig. 1. HiRISE images of a variety of gullies on Mars. Image credits: NASA/JPL/UofA. (a) Gullies on the wall of a small impact crater within Kaiser Crater, site KC in this study, image number: PSP_003418_1335, at 18.8°E, 54.3°S. (b) Gullies within a polar pit, image number: PSP_003498_1090 at 1.6°E, 70.6°S. (c) Gullies on the wall of Galap Crater, near Sirenum Fossae, image number: PSP_003939_1420, at 192.9°E, 37.7°S. (d) Gullies on the wall of Wirtz Crater, a large impact crater to the east of Argyre basin, image number: PSP_002457_1310, at 335.3°E, 48.2°S. (e) Gullies on the slip face of dunes in Russell Crater, located in Noachis Terra, image number: PSP_001440_1255, at 12.9°E, 54.2°S. (f) Gullies on the wall of an impact crater to the west of Newton Crater in Terra Sirenum, image number: PSP_005930_1395, at 196.8°E, 40.3°S.

Fig. 2. Slope-area and Cumulative Area Distribution (CAD) plots, showing typical process domains on Earth. (a) Slope-area plot from Montgomery & Foufoula-Georgiou (1993) with the additional domain of Brardinoni & Hassan (2006) indicated with a dashed line. The arrows and dotted line indicate the adjustment to the alluvial domain boundary considering the gravitational acceleration of Mars. (b) CAD plot from McNamara *et al.* (2006). P(A>A*) represents the probability of a point in the landscape having a drainage area greater than the given drainage area, A*, on the x-axis. Region 1a represents hillslopes that diverge and do not gather drainage. Region 1b represents hillslopes with convergent topography. Region 1c represents pore-pressure triggered landsliding or debris flow. Region 2 represents incision, or channel formation. Region 3 has large steps where large tributaries join the channel.

1308   Fig. 3. Hillshade representations made from digital elevation models of the study site

1309   locations on Earth. Areas included in this study are outlined and labelled in the Figure. (a)

1310   and (b) Site SJ, San Jacinto, California. (c) Site DV, Death Valley, California. (d) Site KA, St

1311   Elias Mountains, Alaska. (e) and (f) Site FR, Front Range, Colorado. (g) and (h) Site WF,

1312   Westfjords, NW Iceland.

1313

1314   Fig. 4. Hillshade representations made from digital elevation models of the study site

1315   locations on Mars. Areas included in this study are outlined and labelled in the Figure. (a) and

1316   (b) Site PC, Penticton Crater in Eastern Hellas. (c), (d) and (e) Site GC, Gasa Crater in Terra

1317   Cimmeria.(f) Site KC, a crater inside Kaiser Crater in Noachis Terra. (g) Site TS, a crater in

1318   Terra Sirenum. (h) The 10 km diameter synthetic crater, in which the square area is where the

1319   pink noise has been applied.

1320

1321   Fig. 5. Close-up views of gullies in Kaiser Crater (site KC), subset of HiRISE image

1322   PSP_003418_1335. Image credits: NASA/JPL/UofA. (a) Examples of gullyheads identified

1323   for individual slope-area analysis, marked by circles containing white crosses. (b) Levées

1324   interior to a channel, arrows point to levées within the channel on each side. (c) Single leveed

1325   channel, arrows point to the more obvious levee on the right, but there is an indication that

1326   there is another on the left as well.

1327

1328   Fig. 6. Slope-area plots for the study areas on Earth. Marked with solid grey lines are the

1329   domains of Montgomery & Foufoula-Georgiou (1993) and Brardinoni & Hassan (2006), as

1330   shown in Fig. 2a. Labels are included in (a), but omitted for clarity in the other plots and are

1331   as follows: (i) hillslopes domain, (ii) debris flow dominated channels, (iii) unchanneled

1332   valleys, (iv) alluvial channels and (v) debris flow deposition domain. The horizontal dotted

1333   line represents the threshold for unconsolidated dry mass wasting at 0.7 gradient, which is

1334   equivalent to 35° slope.

1335   (a) Plots for those areas dominated by talus and creep processes. (b) Plots for those areas

1336   dominated by debris flow, with some influence from talus processes. (c) Plots for those areas

1337   dominated by debris flow, with influence from alluvial processes. (d) Plots for those areas

1338   dominated by ephemeral water flow, or alluvial processes.

1339

1340   Fig. 7. Cumulative Area Distribution plots for the study areas on Earth. (a) Plots for those

1341   areas dominated by talus and creep processes. (b) Plots for those areas dominated by debris

1342   flow, with some influence from talus processes. (c) Plots for those areas dominated by debris

1343   flow, with influence from alluvial processes. (d) Plots for those areas dominated by

1344   ephemeral water flow, or alluvial processes.

1345

1346   Fig. 8. Slope-area plots for the study areas on Mars. Marked with solid grey lines are the

1347   domains of Montgomery & Foufoula-Georgiou (1993) and Brardinoni & Hassan (2006), as

1348   shown in Fig. 2a. Labels are included in (a), but omitted for clarity in the other plots and are

1349   as follows: (i) hillslopes domain, (ii) debris flow dominated channels, (iii) unchanneled

1350   valleys, (iv) alluvial channels and (v) debris flow deposition domain. The horizontal dotted

1351   line represents the threshold for unconsolidated dry mass wasting at 0.7 gradient, which is

1352   equivalent to 35° slope. The dash-dot line represents the adjustment of the alluvial domain

1353   when taking into account Mars' gravitational acceleration. (a) Plots for Site PC, Penticton

1354   Crater in Eastern Hellas. (b) Plots for Site GC, Gasa Crater in Terra Cimmeria. (b) Plots for

1355   Site KC, a crater inside Kaiser Crater in Noachis Terra. (d) Plots for Site TS, a crater in Terra

1356   Sirenum and the 10 km diameter synthetic crater.

1357

1358   Fig. 9. Cumulative Area Distribution plots for the study areas on Mars. (a) Plots for Site PC,

1359   Penticton Crater in Eastern Hellas. (b) Plots for Site GC, Gasa Crater in Terra Cimmeria. (b)

1360   Plots for Site KC, a crater inside Kaiser Crater in Noachis Terra. (d) Plots for Site TS, a crater

1361   in Terra Sirenum and the 10 km diameter synthetic crater.
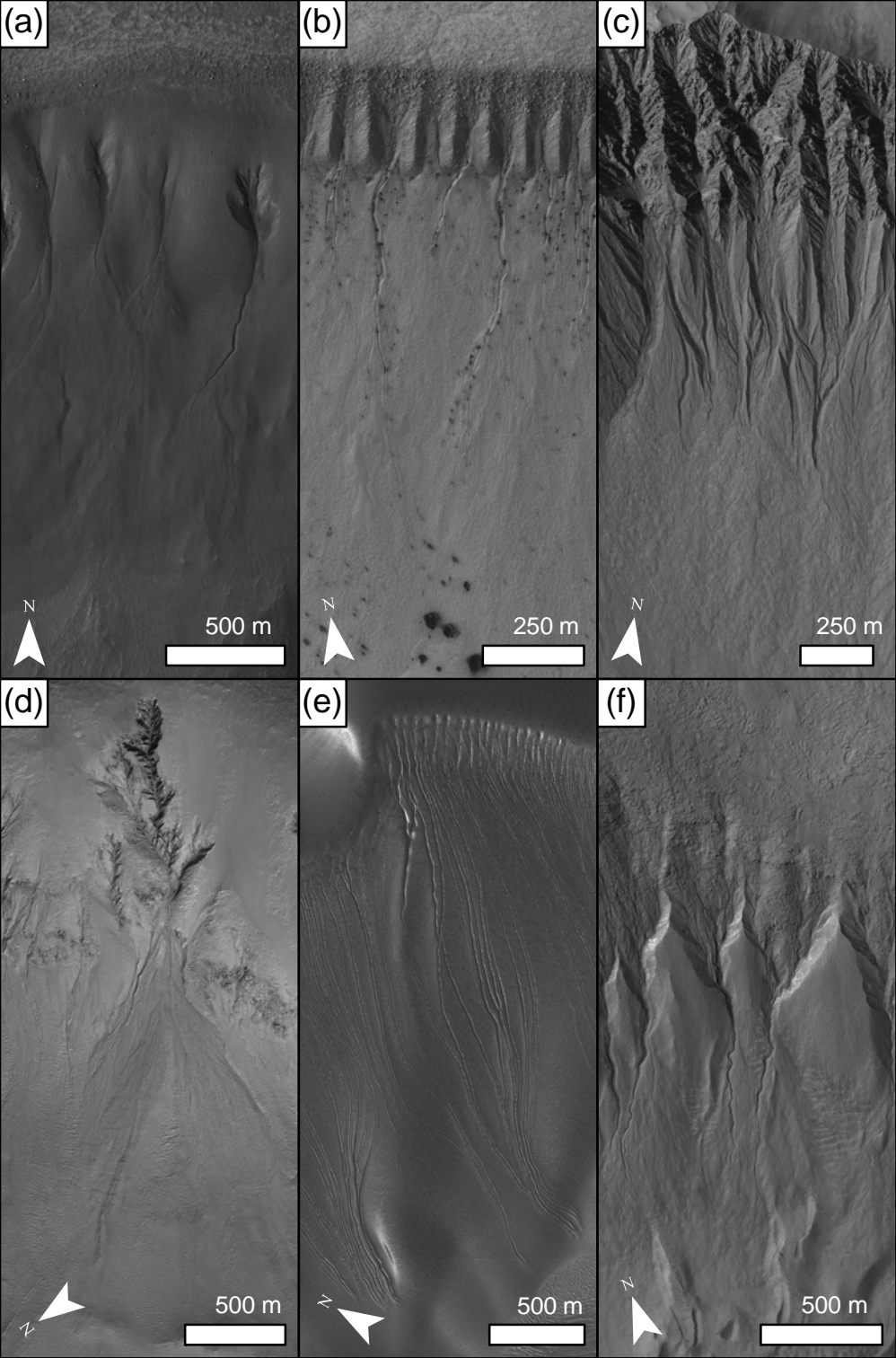
1362

1363   Fig. 10. Wetness index maps made from digital elevation models of the study site locations

1364   on Earth. Areas included in this study are outlined and labelled in the Figure. Wetness index

1365   values are represented by the same colours in Fig. 11 to allow direct comparison. (a) and (b)

1366   Site SJ, San Jacinto, California. (c) Site DV, Death Valley, California. (d) Site KA, St Elias

1367   Mountains, Alaska. (e) and (f) Site FR, Front Range, Colorado. (g) and (h) Site WF,

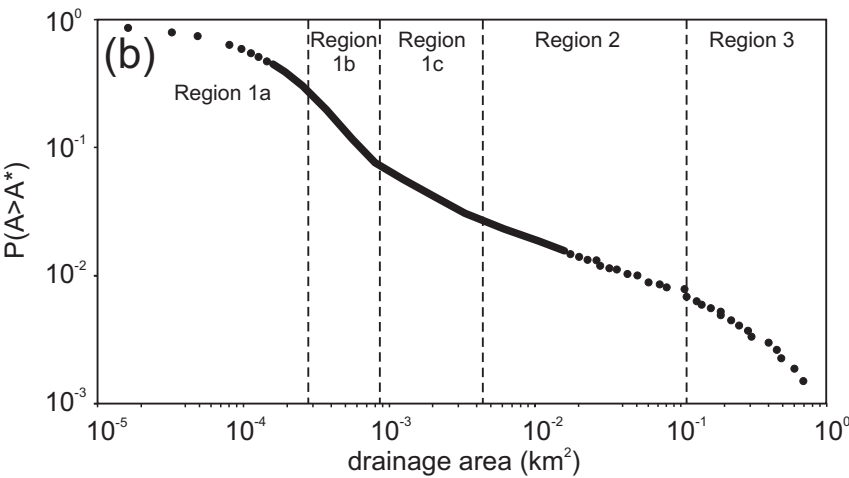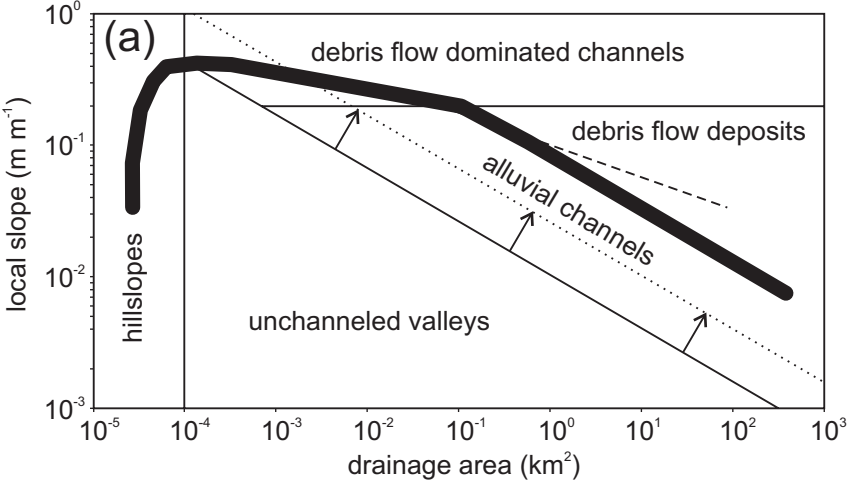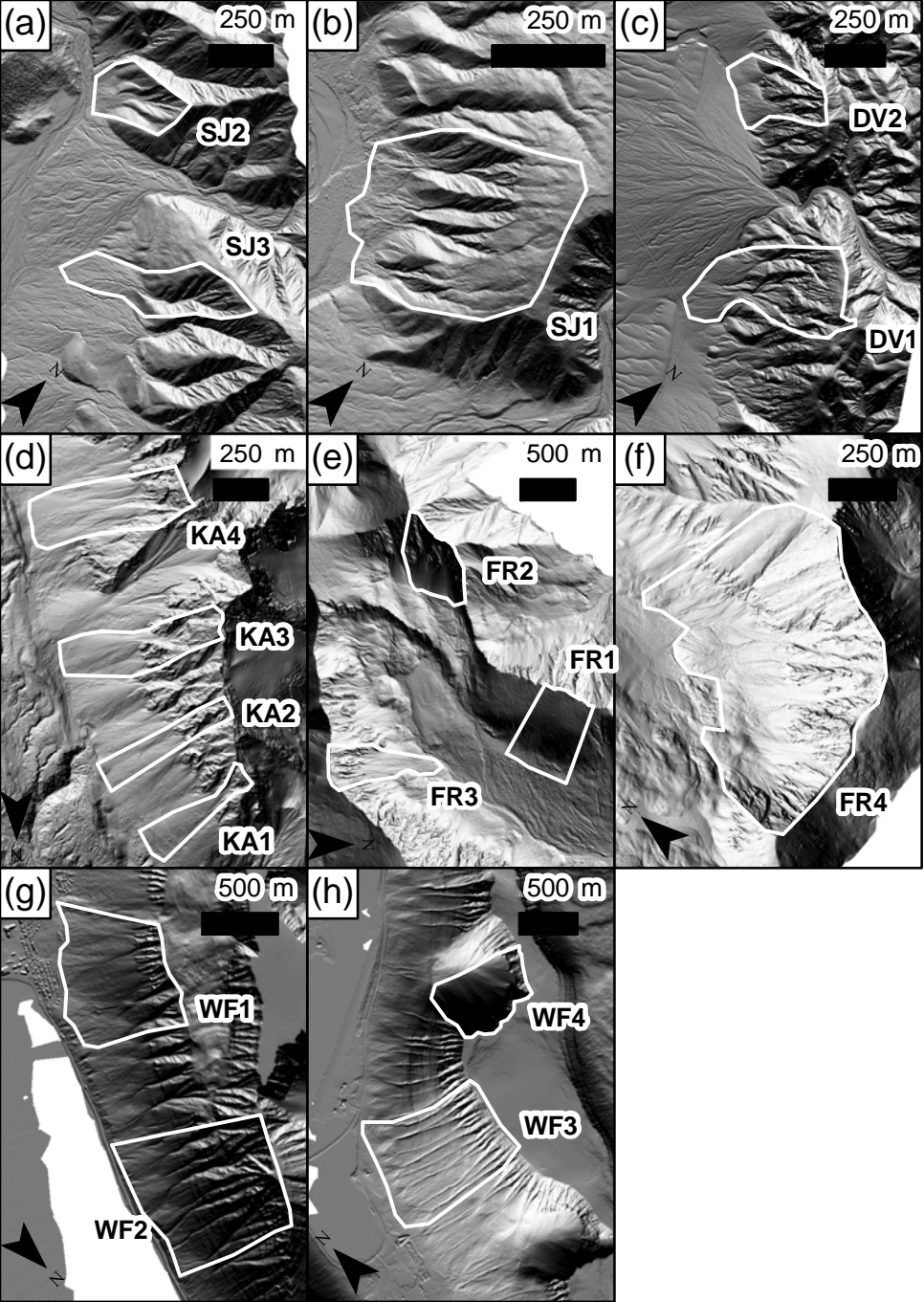1368   Westfjords, NW Iceland.

1369

1370   Fig. 11. Wetness index maps made from digital elevation models of the study site locations

1371   on Mars. Areas included in this study are outlined and labelled in the Figure. Wetness index

1372   values are represented by the same colours in Fig. 10 to allow direct comparison. (a) and (b)

1373   Site PC, Penticton Crater in Eastern Hellas. (c), (d) and (e) Site GC, Gasa Crater in Terra

1374   Cimmeria.(f) Site KC, a crater inside Kaiser Crater in Noachis Terra. (g) Site TS, a crater in

1375   Terra Sirenum. (h) 10 km diameter synthetic crater.

1376

1377

(a) 500 m, N

(b) 250 m, N

(c) 250 m, N

(d) 500 m, N

(e) 500 m, N

(f) 500 m, N

(a) debris flow dominated channels, debris flow deposits, alluvial channels, unchanneled valleys, hillslopes

(b) Region 1a, Region 1b, Region 1c, Region 2, Region 3

(a) PC1 — N — 500 m

(b) PC2 — N — 250 m

(c) GC1 — GC2 — N — 500 m

(d) GC3 — N — 500 m

(e) GC4 — N — 250 m

(f) KC3 — KC4 — KC1 — KC2 — N — 500 m

(g) TS1 — N — 250 m

(h) 500 m

(a) 100 m   N

(b) 10 m

(c) 10 m

Drainage Area (km²)

(a) PC1: Penticton Crater - north facing
PC2: Penticton Crater - west facing

(i) (ii) (v) (iii) (iv)

(b) GC1: Gasa Crater - single SW-facing
GC2: Gasa Crater - group SW facing
GC3: Gasa Crater - south facing
GC4: Gasa Crater - north facing

(c) KC1: Kaiser - single south-facing
KC2: Kaiser - double south-facing
KC3: Kaiser - gullied slope section
KC4: Kaiser - ungullied slope section
Kaiser - gully heads

(d) TS1: unnamed crater - north facing
Synthetic crater slope

Local slope (m m⁻¹)

Drainage Area (km²)

(a)
PC1: Penticton Crater - north facing
PC2: Penticton Crater - west facing

(b)
GC1: Gasa Crater - single SW-facing
GC2: Gasa Crater - group SW facing
GC3: Gasa Crater - south facing
GC4: Gasa Crater - north facing

(c)
KC1: Kaiser - single south-facing
KC2: Kaiser - double south-facing
KC3: Kaiser - gullied slope section
KC4: Kaiser - ungullied slope section

(d)
TS1: unnamed crater - north facing
Synthetic crater slope

P(A*>A)

Wetness index

High : 10

Low : 2

Study areas

(a) PC1 — N — 500 m

(b) PC2 — N — 250 m

(c) GC1, GC2 — N — 500 m

(d) GC3 — N — 500 m

(e) GC4 — N — 250 m
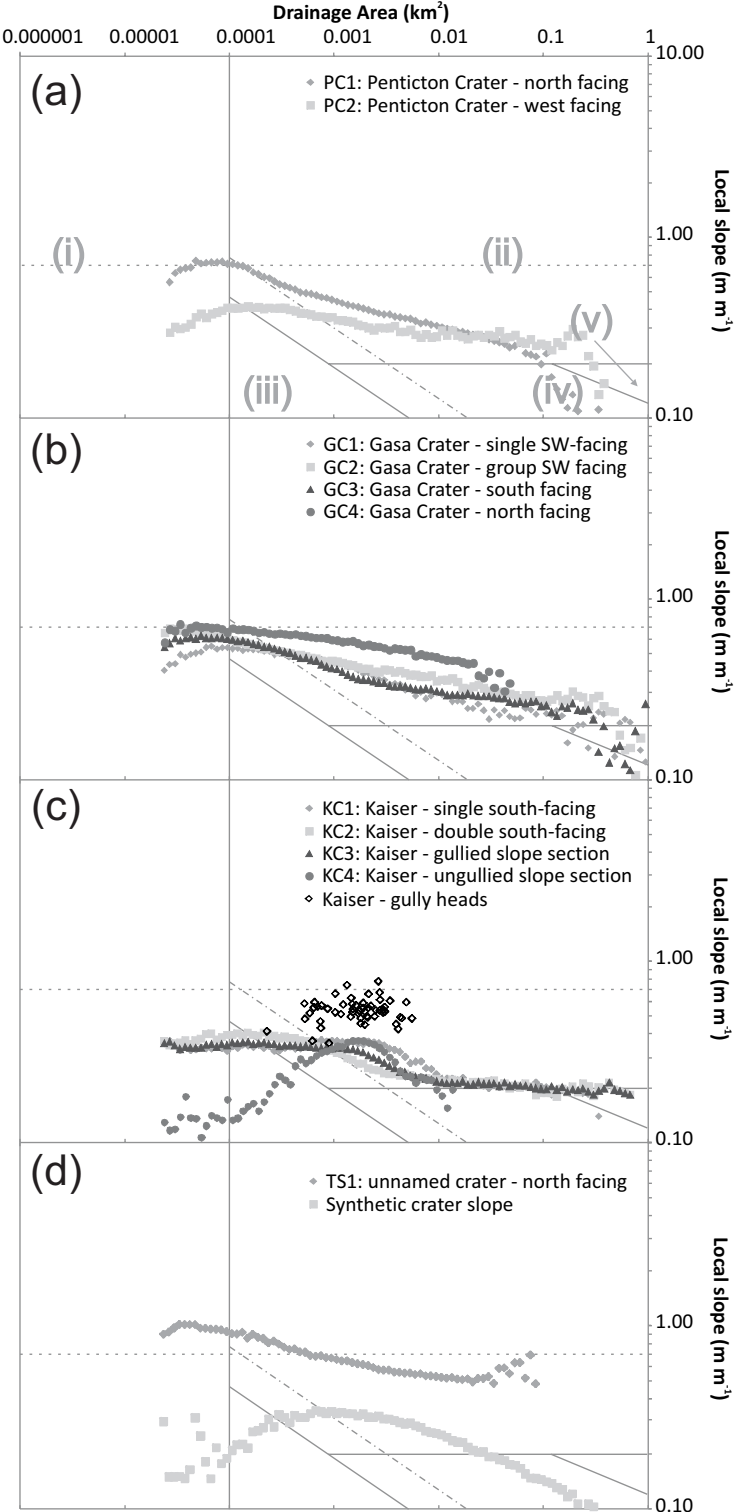
(f) KC3, KC4, KC1, KC2 — N — 500 m

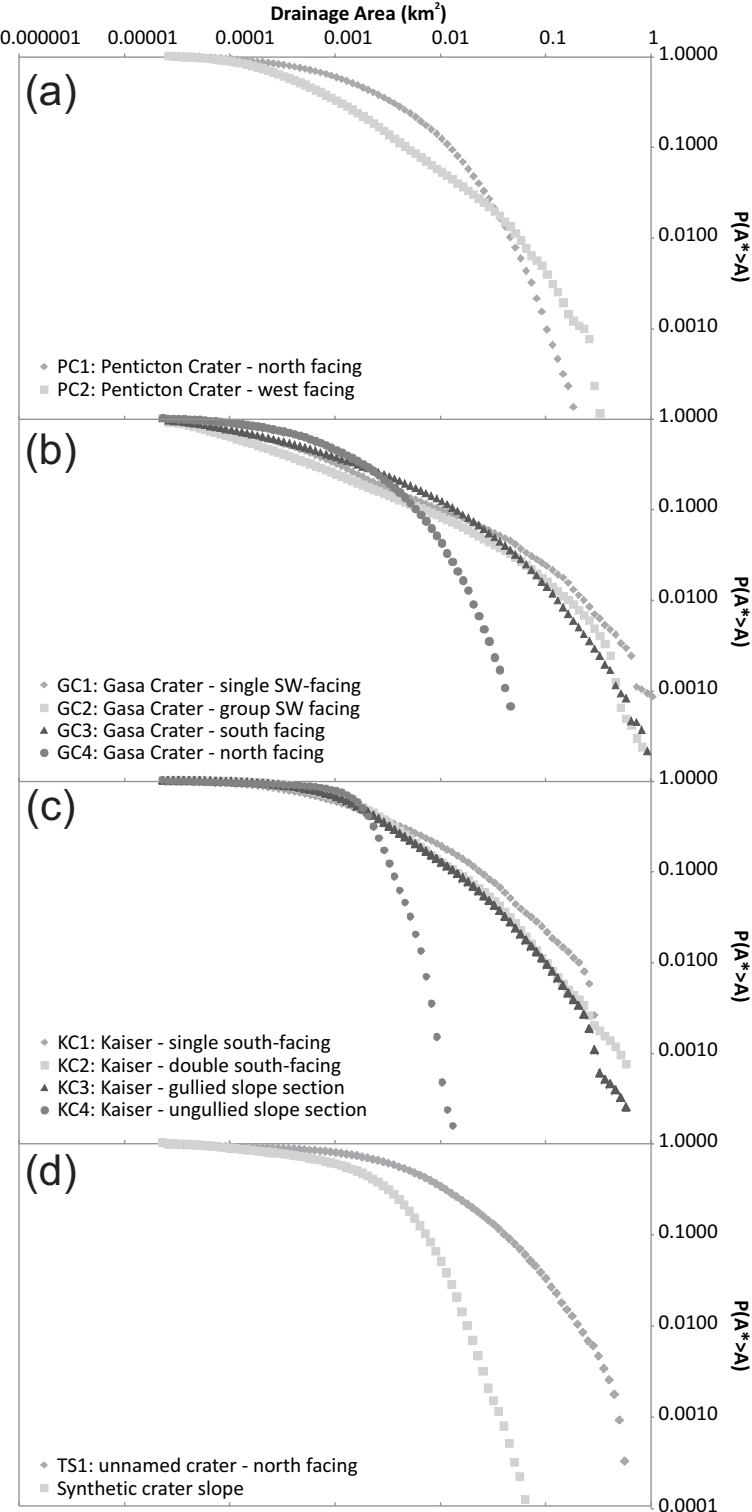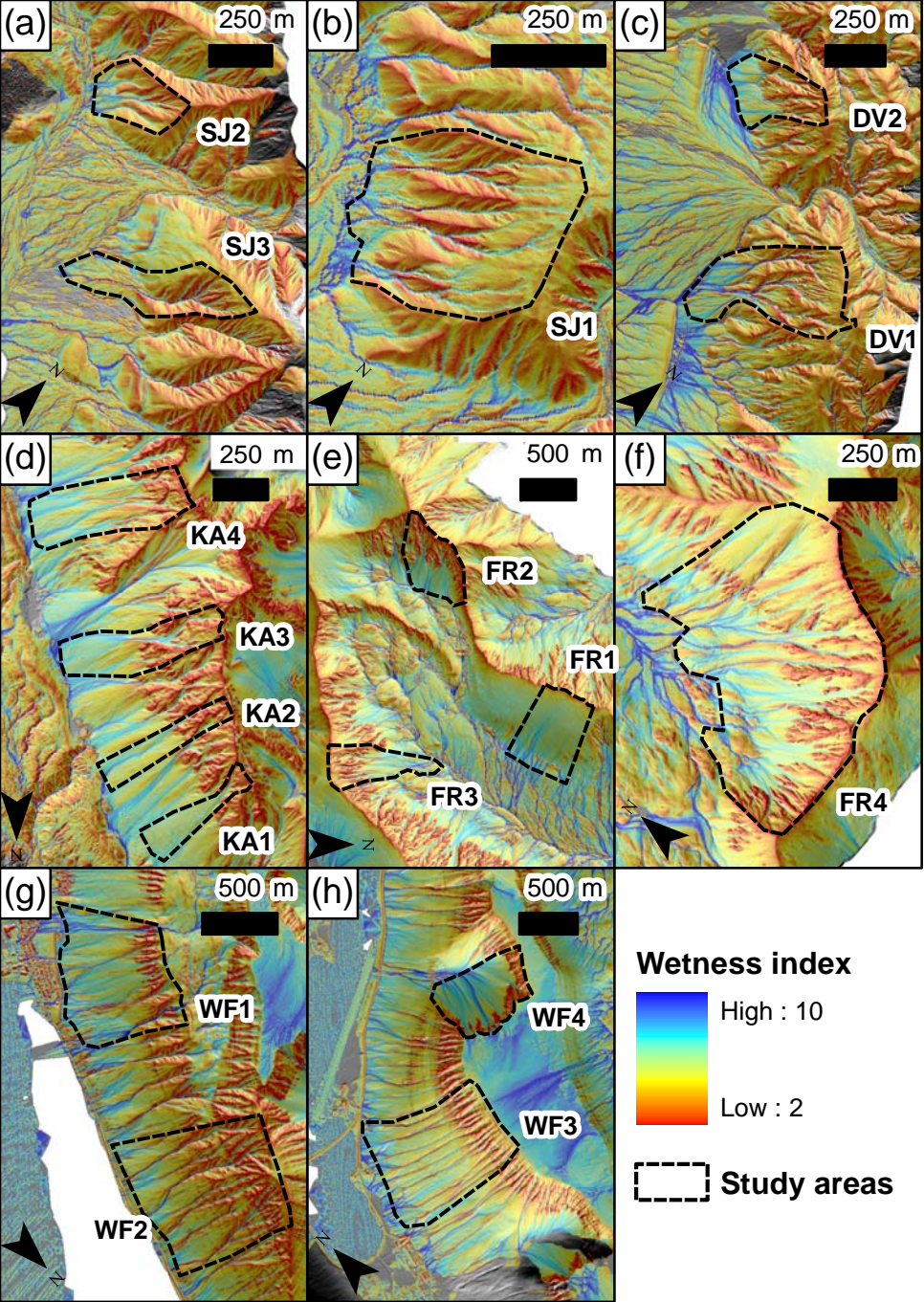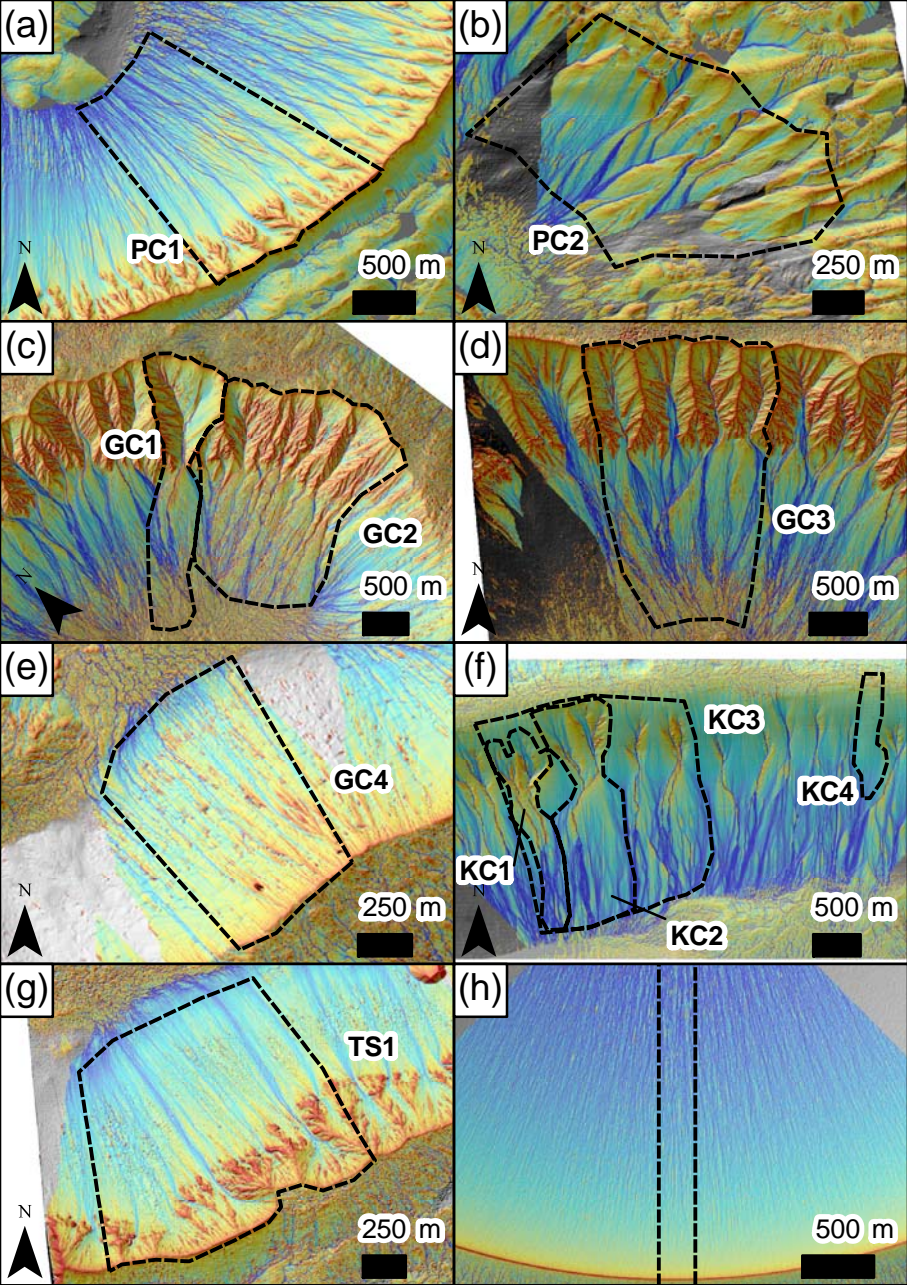(g) TS1 — N — 250 m

(h) — 500 m

Wetness Index: 10 — 2

Table 1. *Summary table for the study sites on Earth*

Site	Location	Date Flown	Data Source	Approx. precipitation (mm/year)	Landscape-type	Latitude	Longitude	Average elevation (m)	Relief (m)
A	San Jacinto Fault (SJF Segment 3) - Santa Rosa Mountains	mid 2005	NCALM B4 Project	150	desert	33° 25' 58.55" N	116° 28' 57.55" W	597	677
B	Death Valley California	28/02/2005	NCALM	<85	desert	39° 38' 01.77" N	105° 49' 13.88" W	3664	1345
C	St. Elias, Alaska	02-15/9/2005	NCALM	2000	periglacial	60° 18' 18.59" N	144° 32' 14.98" W	490	831
D	Front Range, Colorado	30/09/2005	NCALM	600	periglacial	37° 04' 28.50" N	117° 26' 37.60" W	258	854
E	Westfjords, Iceland	05/08/2007	ARSF	700	periglacial	66° 04' 13.20" N	023° 07' 14.19" W	271	807

Average elevation is given relative to datum, for A-D this is NAD 1983 and for Site E this is WGS 1984, in both cases the difference between the datum and sea level is approximately 60 m. Abbreviations: NCALM - National Center for Airborne Laser Mapping supported by the USA's National Science Foundation, ARSF – Airborne Research and Survey Facility supported by the UK Natural Environment Research Council.

Table 2. *Summary table for the study sites on Mars*

Site	HiRISE image pair	Latitide	Longitude	Average elevation (m)	Relief (m)
F	PSP_001714_1415 PSP_001846_1415	-38.4°	96.8°	-2648	1124
G	PSP_004060_1440 PSP_005550_1440	-35.7°	129.4°	300	1205
H	PSP_003418_1335 PSP_003708_1335	-46.1°	18.8°	595	687
J	PSP_003674_1425 PSP_005942_1425	-37.4°	229.0°	1904	961

.

Average elevation is given relative to the Mars datum, as defined from the MOLA dataset. The average elevation has been estimated from the MOLA dataset and relief from the HiRISE DEMs.